

SHARPENING OF CONDUCTIVE NANOPROBES FOR SCANNING TUNNELING  
MICROSCOPY BY FIELD-DIRECTED SPUTTER SHARPENING

BY

SCOTT W. SCHMUCKER

B.S., Case Western Reserve University, 2004

THESIS

Submitted in partial fulfillment of the requirements  
for the degree of Master of Science in Electrical and Computer Engineering  
in the Graduate College of the  
University of Illinois at Urbana-Champaign, 2009

Urbana, Illinois

Advisor:

Professor Joseph W. Lyding

## **ABSTRACT**

This thesis presents a novel sputter erosion sharpening technique for the production of conductive probes on nanometer and atomic scales. This field-directed sputter sharpening procedure is shown to reliably sharpen both tungsten and platinum-iridium alloy probes and to produce atomic-scale topological changes, distinct from traditional sputter erosion sharpening. Possible justification for this effect is presented in the form of controlled ion current modulation at the probe apex. Furthermore, the probes are found to facilitate high-fidelity patterning of the hydrogen passivated silicon surface.

## ACKNOWLEDGMENTS

My tenure at the University of Illinois has been formative, in large part due to the uniquely inspiring atmosphere cultivated by Professor Joseph Lyding. I thank Joe for his guidance and insight, but also for the freedom he has given me to work creatively and collaboratively and to develop my research fields. It remains a joy to work with Joe and to develop as a researcher both through individual perseverance and from Joe's extensive experience and keen insight.

My days in the Illinois STM group might have proved unproductive without the camaraderie and support of my fellow sojourners. Among these, I would first thank those students who assisted directly with the field-directed sputter sharpening project: Aditya Gupta, Daniel Lukman and Eric Lee. Additionally, I am indebted to Dr. Matt Sztelle for his guidance in the mysterious ways of UHV systems and lab operations, as well as his pasta sauce and many games of racquetball. Dr. Laura Ruppalt offered her valuable knowledge of the "Chamber A" system and trained me on its use. No member of the Lyding lab has left without imparting useful knowledge to me, and I thank all current and former lab members for their contributions to my development: Dr. Peter Albrecht, Dr. Josh Ballard, Dr. Erin Carmichael, Dr. Kyle Ritter, Sumit Ashketar, Kevin He, Kyong Hee Joo, Justin Koepke, Pam Martin, Marie Mayer, Peter Ong, Alan Rudwick, Greg Scott, Aditya Vaidya, Bryan Walker, Josh Wood, Wei Ye, and Fan Zhang.

Several other members of the Illinois community played integral roles in the success of my research program. Specifically Scott Robinson and Cate Wallace have repeatedly contributed their expertise and enthusiasm for the transmission electron

microscopy system employed in this work. The Imaging Technology Group of the Beckman Institute at the University of Illinois maintains an excellent microscopy facility which has proven invaluable in the completion of my research. Also, the expert machining skills of Craig Zeilenga have created much of the equipment employed in the Lyding lab. Our group secretary, Kelly Young, and Suzie Rook of the Beckman Institute have contributed continually to the successful operation of the laboratory.

While the Lyding lab brought me to the cornfields of Illinois, it was Professor Daniel Saab of Case Western Reserve University who encouraged me to consider the venerable institution. During my tenure at Case I began work on a joint BS/MS degree program, during which Professor Saab served as my research and academic advisor. Though graduate study drew me away from this program, I thank Professor Saab for his guidance and assistance in a decisive phase of my life. It was a distinct honor to have worked with him, and his insight has been crucial in the development of my research skills.

I graciously acknowledge the financial support of a National Defense Science and Engineering Graduate Fellowship from the Air Force Office of Scientific Research (2004-2007), and the National Science Foundation Graduate Research Fellowship (2007-2009). This research was funded by the Office of Naval Research under grant number N000140610120.

I thank my parents, my sister April, my beloved daughter Lydia, and my family and friends for their love and support in this and in all things. Finally, I thank my wife Christine. As the effort and burden is shared with her, so too is this thesis, as are all my works.

## TABLE OF CONTENTS

CHAPTER 1 INTRODUCTION.....	1
CHAPTER 2 METALLIC PROBES SHARPENED BY FIELD-DIRECTED SPUTTER SHARPENING AND CHARACTERIZED BY TRANSMISSION ELECTRON MICROSCOPY.....	20
CHAPTER 3 MECHANISM OF PROBE NANOSTRUCTURING UNDER FIELD-DIRECTED SPUTTER SHARPENING.....	31
CHAPTER 4 SCANNING TUNNELING MICROSCOPY AND HIGH FIDELITY ELECTRON-STIMULATED DESORPTION.....	39
CHAPTER 5 CONCLUSIONS AND FUTURE WORK.....	46
REFERENCES.....	48
AUTHOR'S BIOGRAPHY.....	51

# CHAPTER 1

## INTRODUCTION

### 1.1 Motivation

As device fabrication techniques draw nearer the limits of scaling in electronic and mechanical systems, we are faced with an intriguing atomic limit of precision. With the invention of the scanning tunneling microscope<sup>1</sup> and subsequent development of scanned probe technologies<sup>2</sup> it has become increasingly possible to discuss a new generation of structures and devices that are fabricated with near-atomic accuracy.

Lyding et al. have demonstrated their ability to produce chemically reactive patterns on the hydrogen passivated silicon surface using electron-stimulated desorption of hydrogen.<sup>3</sup> This desorption method was further extended to the controllable desorption of individual hydrogen atoms by Hersam et al. using feedback controlled lithography.<sup>4</sup> Numerous applications for such patterning techniques have been demonstrated, including the controlled inclusion of individual dopant atoms in silicon,<sup>5</sup> and the production of dangling bond quantum-dot cellular automata structures.<sup>6</sup> These techniques provide nanometer scale patterning resolution, and feedback controlled lithography provides precise control over the number of atomic desorption events. Nevertheless, electron-stimulated modification techniques are inherently stochastic in nature, with patterning fidelity dependent on the spatial distribution of electron tunneling current between tip and sample. In the case of electron-stimulated desorption, this effect appears as spurious depassivation events in the pattern vicinity, in the tail of the electron current distribution. Reliable achievement of atomically precise control, where the electron tunneling distribution is well confined within atomic proportions, promises the

ultimate limit of scaling at which each atomic element is precisely controlled and structures are manufactured identically and reproducibly to the limits of our theoretical ability.

While the scanning tunneling microscope offers the potential to this goal, its ability to reliably and reproducibly form device structures is dependent on our ability to provide reliable and reproducible atomic-scale probes that form the core of scanned probe instruments. As a result, one necessary goal remains the production of atomically sharp and *reproducible* metallic probes. This thesis presents the field-directed sputter sharpening process, a novel sputter erosion sharpening technique which seeks to further the ability to achieve the goal of high fidelity atomic-scale manufacturing.

## **1.2 Probe Sharpening Methodology**

The sharpening of conductive probes is a broad field of research, commonly enmeshed with the study of electron beam sources for electron microscopy,<sup>7</sup> field emitter arrays for display applications,<sup>8</sup> and atomic probes for scanned probe microscopy.<sup>9</sup> The field has increasingly flourished since the advent of the scanning tunneling microscope,<sup>1</sup> an application generally dependent on the detailed structure of a scanned probe. Sharpening techniques have been the focus of book chapters<sup>10</sup> and review articles.<sup>11</sup> The techniques employed in this work and the progression of sputter sharpening technology will be detailed. When quantifying the microstructure of a probe, a practice of measuring radius of curvature and cone angle will be adopted. As the cone angle may vary with length scale, we take this angle to refer generally to the angle of the smallest defined cone, proximally nearest the probe apex. A definition of these characteristics is

shown schematically in Figure 1.1. In the literature, this method of quantifying tip form is commonplace, though in some cases the apex diameter is referenced, and defined as the width of the smallest distinguishable apex feature.<sup>12</sup> The term “cone angle” is frequently applied interchangeably with the “cone half-angle,” which is half of the cone angle described in this thesis.

### **1.2.1. Electrochemical etching of metallic probes**

Most probe materials routinely employed offer well understood chemical or electrochemical etch procedures for production of sharp microtips. In one manifestation, tungsten probes can be etched electrochemically in 3M NaOH or KOH solution under an applied DC bias, while platinum-iridium alloy can be successfully etched in CaCl<sub>2</sub> with an applied AC bias. Additional materials employ varied etchant and biasing conditions and may require subsequent etch steps.<sup>13-15</sup> In all cases, these etching procedures fall routinely into two distinct categories, herein termed “drop-off” and “cut-off” techniques.

Under drop-off, or lamellae, etching<sup>16</sup> the desired probe wire length is extended through an inert counter-electrode ring within which an etchant film is confined. While etching, this probe wire thins and breaks under applied bias, and the released wire is captured for use. All tungsten tips reported in this work were initially etched using the drop-off technique.

Similarly, under the cut-off or emersion technique,<sup>17</sup> several diameters of wire are submerged in an etchant solution in the vicinity of a counter-electrode. For this work, and commonly for platinum-iridium etching, this counter-electrode is composed of graphite.<sup>13,18</sup> In this configuration, a small teardrop forms and detaches from the wire

apex, while the top probe is collected for use. In many cases, cut-off circuitry can be employed to detect this completion event,<sup>17</sup> while in this work some platinum-iridium probes employ a mild fine etch immediately prior to completion to reduce etch rate significantly and allow for manual cut-off. Platinum-iridium probes etched in-house for this work were prepared using the cut-off process described with fine etch and manual cut-off.

### **1.2.2. Conventional sputter erosion sharpening of metallic probes**

Since the discovery of pyramidal microstructure on ion bombarded surfaces,<sup>19</sup> the physics of sputter erosion have been irrevocably linked to probe sharpening. The ability to employ these sputter erosion techniques for the sharpening of probes has been extensively explored.<sup>20-31</sup> The sharpening of polycrystalline tungsten wire is widely reported, with resulting radii of curvature between 5 nm<sup>30</sup> and ~20 nm.<sup>32</sup> The physics of conventional sputter erosion sharpening will be described in detail in Section 1.3.

### **1.2.3. Metallic probe sharpening by the Schiller decapitation process**

Another intriguing technique for sharpening of metallic field emitters was described by Schiller et al.<sup>33</sup> and is herein termed the Schiller decapitation process. Schiller decapitation can be conceptualized as the sputter erosion analog of a cut-off electrochemical etch, under which a metallic tip is modified by self-sputtering. Under Schiller's technique, a negative bias is applied to a tip, inducing field ionization and subsequent sputter erosion of the probe apex and shank. The resulting probes offer a reported radius of curvature between 4 nm and 6 nm. However, the technique requires a

monitored decapitation detection mechanism, limiting the ability of this technique to scale to highly parallelized probe arrays. The Schiller decapitation process is the only example known to the author of a field-influenced sputter erosion process, as the electric field surrounding a biased conductor serves to direct the flux of ions. However, the technique is differentiated from the field-directed sputter sharpening process most clearly by polarity of the applied bias and by the ion source itself. Where the applied negative bias under Schiller decapitation attracts locally generated ions to the probe, under the field-directed sputter sharpening procedure described in Chapter 2 an applied bias repels remotely generated ions, which travel a hyperbolic path away from the probe.

### **1.3 Sputter Erosion Physics**

The study of sputter-induced erosion of materials and the resulting generation of predictable microstructured and nanostructured patterns has been a focus of study for more than 50 years.<sup>34</sup> Study of the stopping of particles in matter and the relation between sputter yield and angle of incidence from which this phenomenon is derived<sup>35</sup> date back further still. In his experimental result of 1959, Wehner demonstrated the sharpening of 0.5 mm diameter metallic spheres following extensive sputter erosion over hundreds of hours.<sup>34</sup> In this early work, similar to those which followed, the spheres are electrically connected to the grounded reference potential. The underlying physics of this sputter erosion are well described by the Sigmund model.<sup>20</sup> Understanding of conventional sputter erosion physics was additionally refined through the work of Barber et al.<sup>21</sup> and Carter et al.,<sup>25</sup> in which the sputter erosion process is treated with Frank's model of chemical dissolution of crystals by kinematic wave theory.<sup>36,37</sup>

In a simplistic model, sputter erosion of surfaces can be envisioned as a flux of energetic ions inducing vibration and displacement of atoms within a substrate by collision cascade.<sup>20</sup> We can describe micro-scale sputter erosion by the sputter yield:

$$Y(\theta) = \frac{\text{atoms ejected}}{\text{incident ion}} \quad (1.1)$$

As expected, the sputter yield is a function of substrate material and structure, ion species, and ion energy. Additionally, the sputter yield exhibits a curious relation to the angle of incidence ( $\theta$ ) between the ion path and the substrate normal line, shown from theoretical modeling in Figure 1.2. When considered in terms of a cascade of atomic collisions and the non-zero penetration depth of each ion (Figure 1.3), this result becomes apparent. Sputter yield is the number of displaced atoms with sufficient recoil action to reach the sample surface and sufficient energy to overcome surface binding forces. As a result, most sputtered atoms are surface atoms, and sputter yield is approximately related to the spatial overlap between the sputter cascade and the substrate surface (Figure 1.4). As the angle of incidence of an incoming ion varies from surface normal to glancing incidence, a greater fraction of energy is distributed along the near-surface plane, increasing the overlap between the energy distribution and surface plane, and therefore increasing the sputter yield. An energetic ion will penetrate the surface while slowing due to the influences of nuclear and electronic stopping. Energy from the ion is distributed within the surface through interaction with atomic nuclei, producing an energy distribution centered at some distance beneath the surface and with a distribution that is approximately Gaussian.<sup>20</sup> As the angle of incidence is increased, sputter yield will increase as overlap between the sputter cascade and the substrate surface increases, thus facilitating the escape of a larger fraction of surface atoms.

Approaching glancing incidence, ion reflection becomes increasingly prevalent, resulting in a rapid sputter yield decline until erosion ceases for ion flux parallel to the surface.

In modeling conventional sputter sharpening, two distinct modes will prove useful. Under the first-order model of sputter sharpening, topographical surface modification is considered on a scale significantly larger than the ion penetration depth. In this case, we can model a sharpening process from the relation between yield and angle of incidence. Modeling first-order conventional sputter sharpening, we consider a probe of distinct, flat planes as shown in Figure 1.5. During sputter erosion, each plane will etch at a rate related to its angle by the  $Y(\theta)$  curve. As competing planes propagate, those etching most rapidly will in time overtake more gradually etched planes, resulting in an arbitrarily sharp apex with cone angle corresponding to the global maximum of the  $Y(\theta)$  curve. Experimentally, this maximum is found to produce cone angles between 60 and 80 degrees for various material substrate and ion species.<sup>38</sup>

This first-order model provides a clear understanding of microstructure produced by sputter erosion well above the nanometer scale, particularly of the probe cone angle. However, in understanding conventional sputter sharpening at the nanometer and sub-nanometer scale, one must more explicitly consider the collision cascade as well as surface diffusion effects.

A second-order model of conventional sputter erosion follows directly from the collision cascade when the spatial extent of this cascade is modeled. From this model, with explicit consideration of the atomic-scale effects within the cascade of influenced lattice atoms, one can derive the effects observed under the first-order erosion model,

specifically the relation between sputter yield and angle of incidence. As described by Sigmund,<sup>23</sup> at the length scale of the collision cascade, sputtering of material from the target surface will preferentially occur downstream from the impact site. Additionally, the model predicts the formation of a depression surrounding the base of an eroded pyramid, a structural effect verified experimentally in the study of sputter-induced morphological changes on surfaces.<sup>39</sup> Sputter erosion is reduced at the probe apex, but enhanced along the neighboring slope, leading to a reduction of cone angle on the length scale of ion penetration.

Such collision-based erosion models do not readily explain the resulting radius of curvature of a probe under conventional sputter sharpening. Ultimately, the sharpening process is limited by the ion penetration depth, and the minimum radius of curvature should be on this scale. Though this fundamental limitation exists, those sputter erosion models described neglect the effect of surface diffusion on the final tip shape. As explained by Carter<sup>24</sup> and Carter et al.<sup>25</sup> in a first-order erosion model, the resulting probe apex is further modified by the influence of thermally induced and radiation enhanced surface diffusion. Following the derivation of Carter,<sup>24</sup> for a two-dimensional system and amorphous substrate in the absence of stress, we can describe the flux of diffusion surface atoms crossing a unit length as

$$J = \frac{DN_0\Omega\gamma}{kT} \frac{\partial}{\partial z} \left( \frac{1}{R} \right) \quad (1.2)$$

where  $D$  is the coefficient of surface diffusion at temperature  $T$ ,  $k$  is Boltzmann's constant,  $N_0$  is surface atomic density,  $\Omega$  is the atomic volume,  $\gamma$  is the surface energy, and  $R$  is the radius of curvature. Taking the divergence of  $J$  and multiplying by the

atomic volume ( $\Omega$ ) we find the rate of erosion or accumulation of material attributed to surface diffusion is given by

$$\left| \frac{\partial n}{\partial t} \right|_D = \frac{DN_0\Omega^2\gamma}{kT} \frac{\partial^2}{\partial z^2} \left( \frac{1}{R} \right) \quad (1.3)$$

Where  $\theta$  is the angle of incidence of an axially oriented ion beam on the surface, the radius of curvature can then be defined as

$$R = -\frac{dz}{d\theta} \quad (1.4)$$

and the rate of erosion attributed to diffusion can be given by

$$\left| \frac{\partial n}{\partial t} \right|_D = -\frac{DN_0\Omega^2\gamma}{kT} \frac{\partial^3 \theta}{\partial z^3} \quad (1.5)$$

Additionally, the erosion rate for sputtered material is given from the ion flux ( $\phi$ ), substrate atom density ( $N$ ) and sputter yield ( $S$ ), accounting for the known cosine dependence on angle ( $\theta$ ) by

$$\left| \frac{\partial n}{\partial t} \right|_T = -\frac{\phi}{N} S \cos \theta \quad (1.6)$$

From here a consolidated erosion rate equation can be written:

$$\left| \frac{\partial n}{\partial t} \right|_T = -\left[ \frac{\phi}{N} S \cos \theta + \frac{DN_0\Omega^2\gamma}{kT} \frac{\partial^3 \theta}{\partial z^3} \right] \quad (1.7)$$

Recalling that  $S$  is the sputter yield at normal incidence, an effective sputter yield,  $S_e$ , is defined such that

$$\left| \frac{\partial n}{\partial t} \right|_T = -\frac{\phi}{N} S_e \cos \theta \quad (1.8)$$

We therefore determine the effective sputter yield, from which sputter erosion and surface diffusion can be modeled on large length scales and incident angles less than the critical angle.

$$S_e = S + \frac{N}{\theta} \frac{DN_0 \Omega^2 \gamma}{kT} \sec \theta \frac{\partial^3 \theta}{\partial z^3} \quad (1.9)$$

It must be noted that such derivation of effective sputter yield neglects the potential for radiation enhanced surface diffusion, whereby the ion flux directly influences the rate of diffusion. Discussed by Carter,<sup>24,26</sup> this effect has been studied in detail by Bradley and Harper<sup>29</sup> and must be considered in the modeling of field-directed sputter erosion.

Whereas sputter erosion tends toward the general reduction of probe radius, the influence is balanced by a preferential flux of diffusing surface atoms from the region of greatest curvature. Such diffusion can be induced by thermal influences, localized or distributed, or by radiation-induced surface self-diffusion, described in detail by Cavaillé and Drechsler.<sup>40</sup> Additionally, the effects of surface diffusion are influenced by the local electric field,<sup>41</sup> further complicating analysis of the sputter erosion process.

#### 1.4 Experimental Setup

The sputter sharpening described in this thesis was performed in the ultrahigh vacuum system shown in Figure 1.6, located within the laboratory of Professor J. Lyding in the Beckman Institute at the University of Illinois Urbana-Champaign. Sputter erosion operations were performed in a high-vacuum antechamber with a nominal base pressure of  $8 \times 10^{-9}$  torr. The chamber is evacuated by a Pfeiffer-Balzars TPU-240 turbomolecular pump backed by an Alcatel 2008A mechanical roughing pump. An integrated ion source is available in the form of a Physical Electronics PHI 04-161

sputter ion gun and corresponding OCI Vacuum Microengineering IPS3 controller. Electrical contact to the probe is provided by dual, high voltage, vacuum feedthroughs that allow for biasing and, where desirable, resistive heating. During field-directed sputter sharpening, tip bias is applied by a Systron-Donner M107 precision DC voltage source adjustable to 1 kV. During sputter cycling the chamber is backfilled to  $5.5 \times 10^{-5}$  torr of argon or neon gas using a Varian leak valve. Chamber pressure is monitored by an in situ nude ionization gauge and Varian Multi-Gauge controller with corresponding UHV board (Gas Correction Factor 1.0).

Probe characterization is performed in a Philips CM200 transmission electron microscope (TEM) operating at 200 kV with nominal achievable resolution of 2 Å. The CM200 includes an integrated CCD camera (2000 x 2000 pixel) for image collection. Prior to TEM characterization, probes are removed to ambient conditions for transfer.

Additionally, the high-vacuum sputter erosion chamber is interlocked with ultrahigh vacuum (UHV) preparation and scanning tunneling microscope (STM) chambers, both maintained below  $1 \times 10^{-10}$  torr, for which the probes are destined. Imaging and patterning work is performed in constant-current mode using a room temperature STM designed by Lyding et al.<sup>42</sup> comprising two concentric piezoelectric tubes. The inner tube provides fine probe motion and facilitates inertial probe translation<sup>43</sup> while the outer tube provides inertial sample translation. Microscope control is accomplished via a digital feedback control system<sup>44</sup> and custom software designed by Professor J. Lyding. An STM system of similar structure is shown schematically in Figure 1.7 and has been described previously.<sup>45</sup>

## **1.5 Thesis Statement**

A novel field-directed sputter sharpening (FDSS) process for the sputter erosion sharpening of conductive probes has been developed and demonstrated for the cases of tungsten and platinum-iridium alloy material systems. The FDSS technique is found to produce sharper probes than conventional sputter erosion techniques employed under equivalent conditions. It is suggested that this effect results from a localized reduction of ion flux at the probe apex facilitated by electric field enhancement at regions of reduced radius of curvature. The resulting reduction in ion flux at the probe apex is simulated in the form of a uniform flux impinging upon an isolated charged sphere.

Also presented are data verifying the imaging and spectroscopic stability and patterning fidelity of FDSS probes in scanning tunneling microscopy and nanolithography. FDSS probes were found to facilitate high precision patterning of the hydrogen passivated silicon (100) surface and to be regenerable in the event of degradation.

## 1.6 Figures

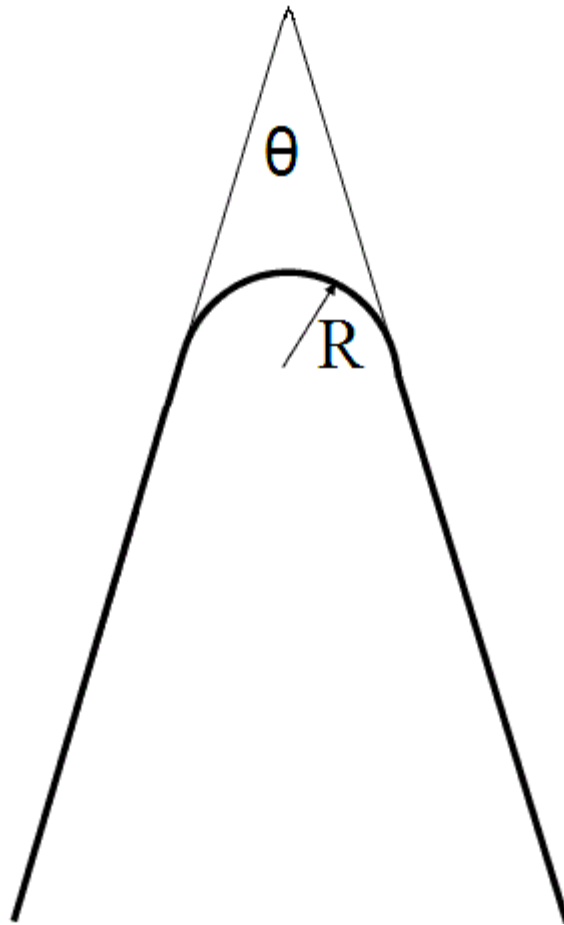


Figure 1.1: Schematic representation of the relevant geometric characteristics of a sharpened probe. The cone angle ( $\theta$ ) and radius of curvature ( $R$ ) completely describe the typical form of the near-apex region of probes processed by sputter erosion sharpening.

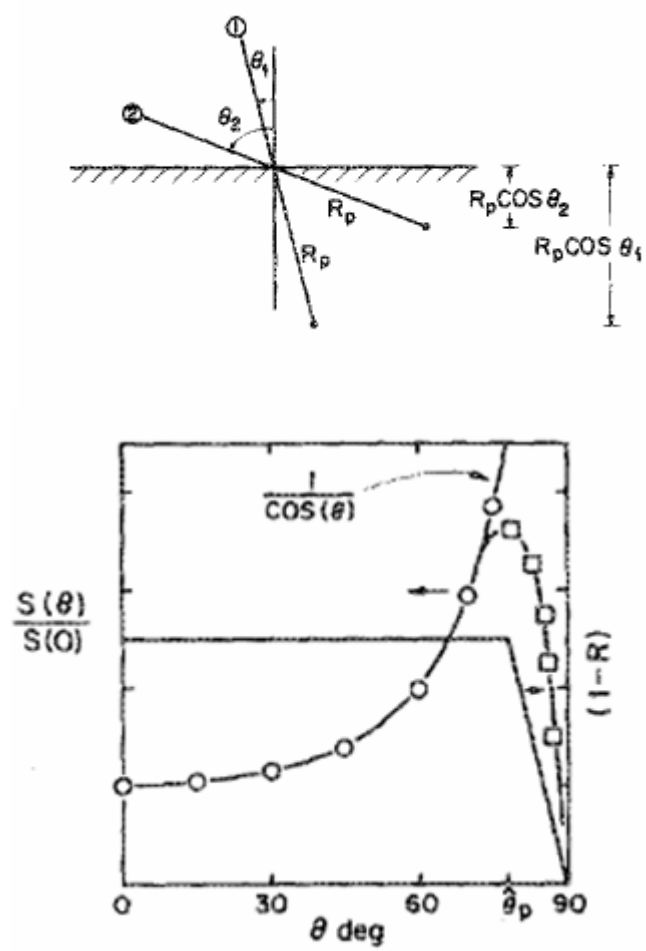


Figure 1.2: Theoretical representation of the dependence of sputter yield on angle of incidence, from reference 27. Figure 1.3a demonstrates the cosine dependence of energy distribution depth on angle of incidence, while Figure 1.3b models this relation for small angles, while displaying a typical peak and decline resulting from the ion reflection coefficient,  $R$ . The angular dependence of sputter yield is shown to increase for increasing angle of incidence, before peaking at critical angle  $\theta_p$  and falling to zero for grazing incidence.

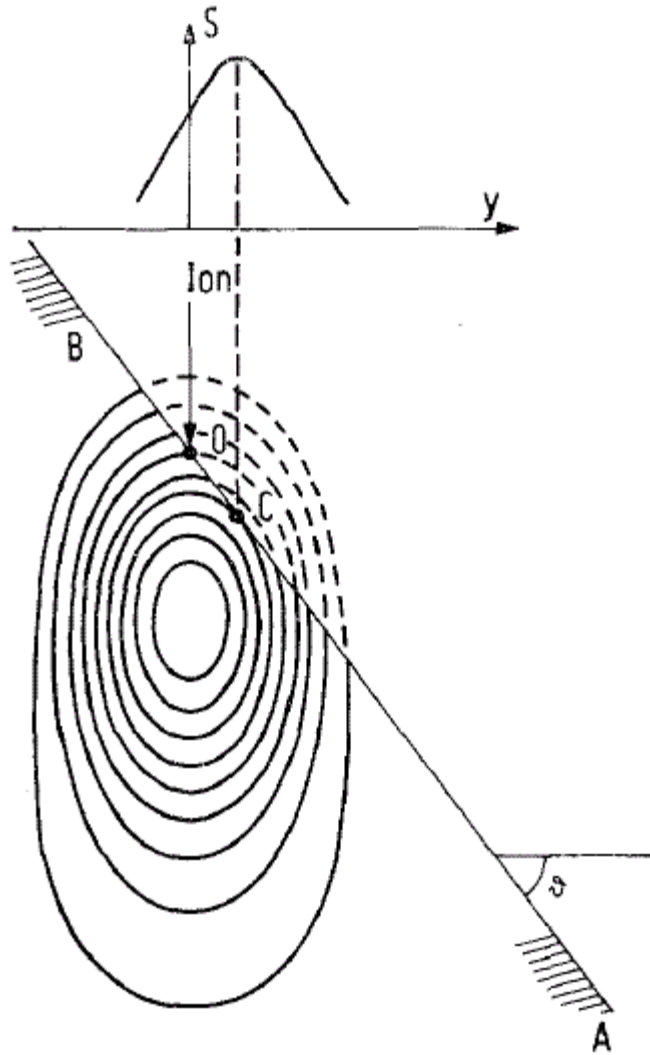


Figure 1.3: Schematic representation of sputter depth profile from reference 23. Sigmund demonstrates the influence of ion penetration depth and the distribution of the sputter cascade on sputter erosion. The offset between the point of ion impact and the point of maximal sputter yield is shown to result.

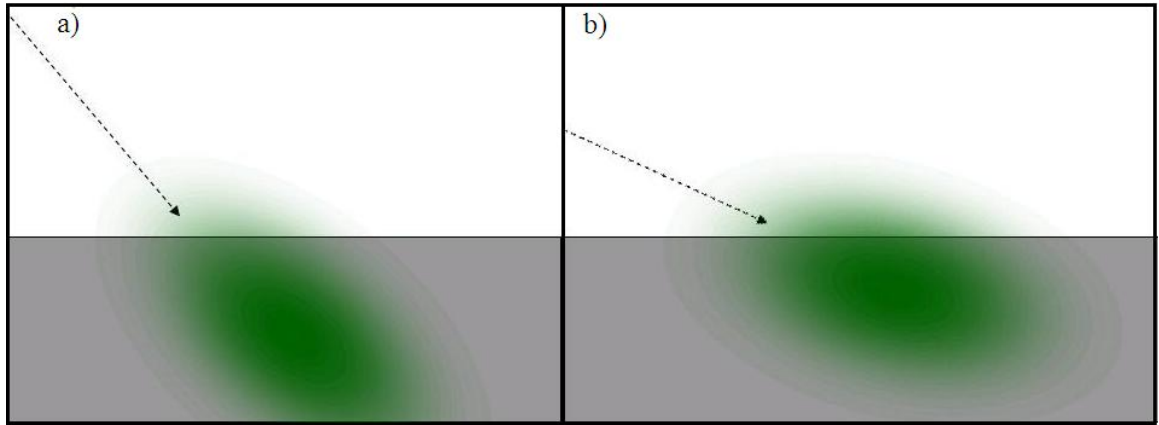


Figure 1.4: Schematic representation of the distribution of ion energy within the target substrate. The arrows demonstrate the path of ion approach for two distinct angles of incidence. The distribution of ion energy is overlaid. Sputtering occurs most frequently at points where the energy distribution and surface overlap. It is seen that this overlap increases when the ion path approaches glancing incidence, leading to the cosine dependence of sputter yield on angle of incidence.

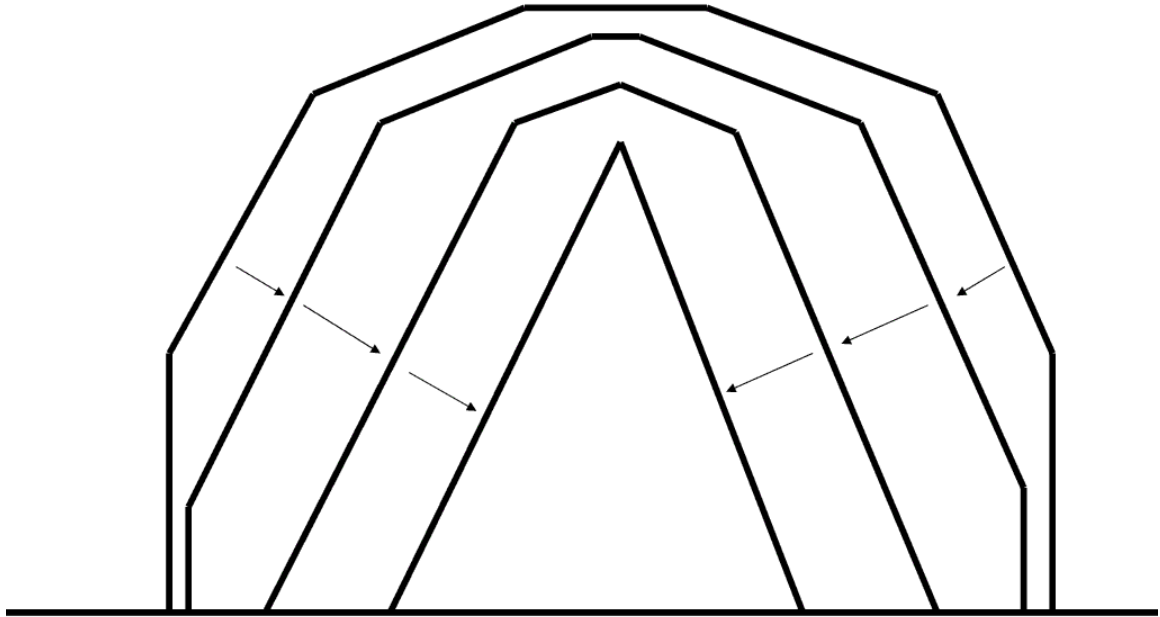


Figure 1.5: A flat-plane representation of first-order sputter erosion sharpening. Each plane erodes at a velocity related to the sputter yield at the corresponding angle of incidence. Ultimately, those planes which translate at maximal velocity are found to supersede all other planes. This provides schematic justification of the prevailing theory that the cone angle of conventional sputter sharpened probes results from the peak of the yield curve.

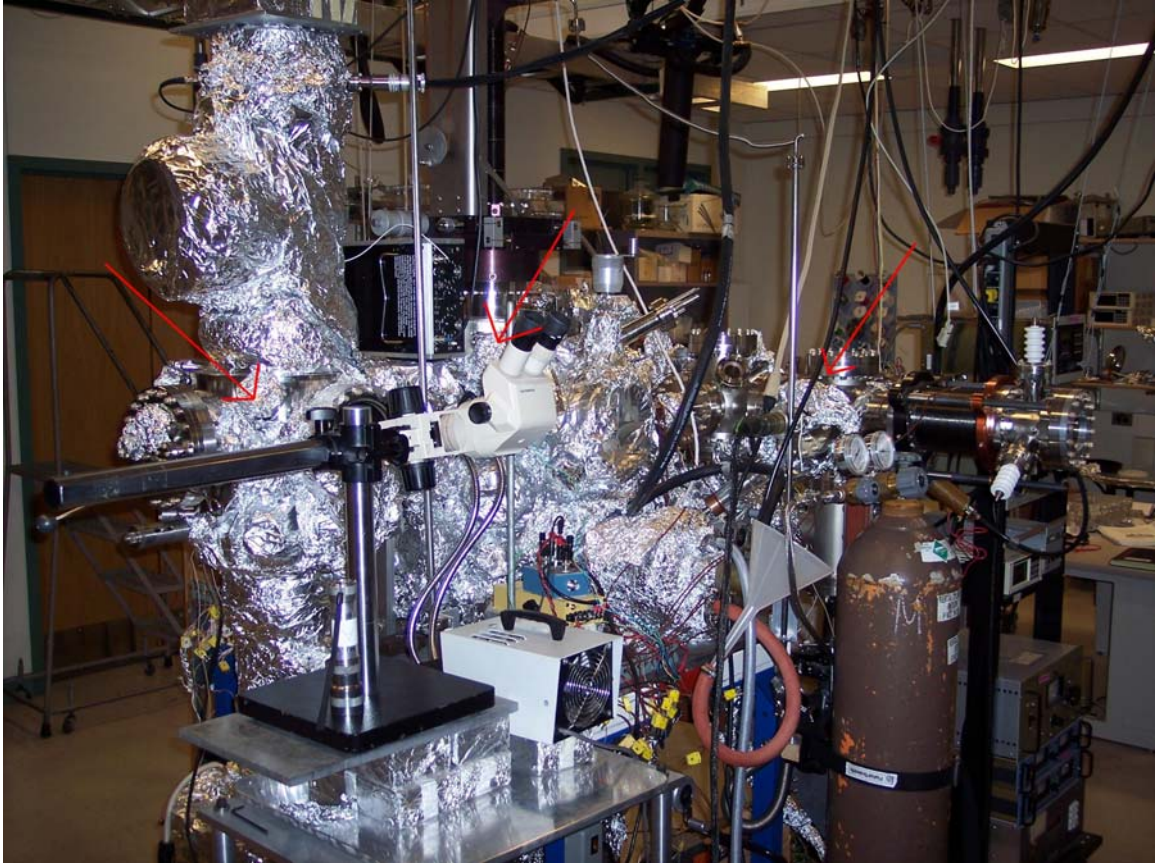


Figure 1.6: The “Chamber A” ultrahigh vacuum system employed in this work. Included and specified are the sputtering chamber where sputter erosion is performed, the preparation chamber where sample and tip cleaning and other preparation techniques are performed, and the scanning tunneling microscope (STM) chamber, where the microscope is located.

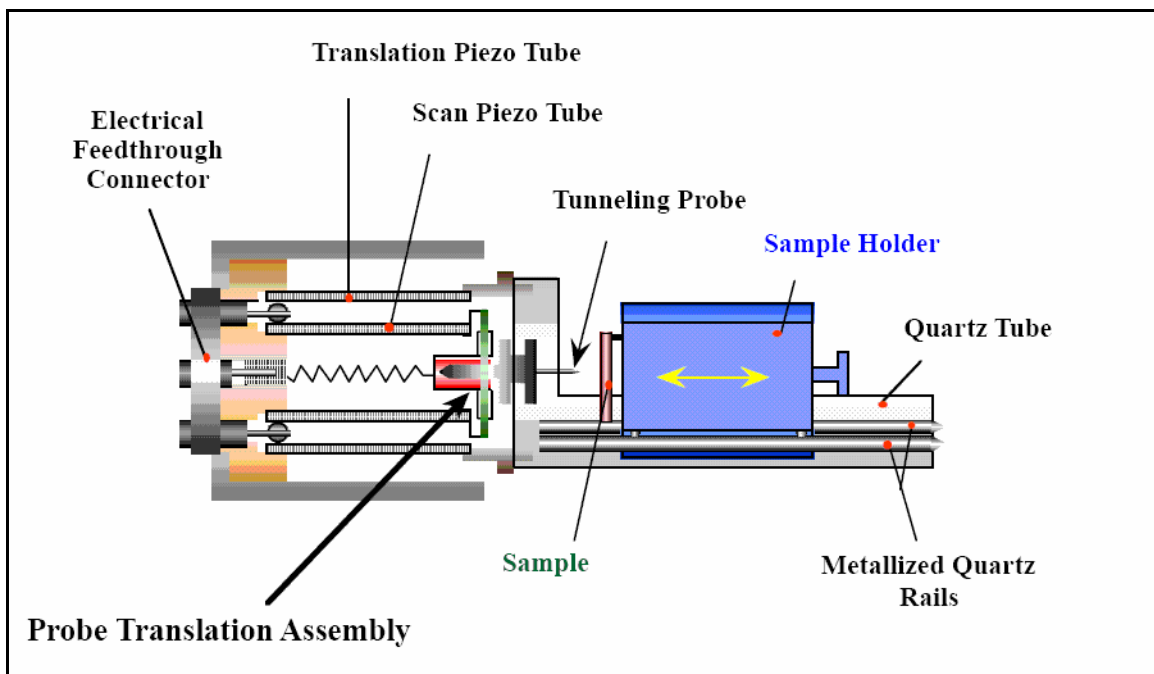


Figure 1.7: A schematic representation of the Lyding model scanning tunneling microscope employed in this work. Diagram courtesy of Professor J. Lyding.

## **CHAPTER 2**

### **METALLIC PROBES SHARPENED BY FIELD-DIRECTED SPUTTER SHARPENING AND CHARACTERIZED BY TRANSMISSION ELECTRON MICROSCOPY**

This chapter presents the results of sputter erosion sharpening of metallic probes in the presence of a controlled electrostatic field at the probe apex. The processing procedure will be detailed for platinum-iridium and tungsten probes, and the results presented and discussed. This manifestation of sputter erosion physics will be discussed in further detail in Chapter 3 and potential explanations specified.

#### **2.1. Field-Directed Sputter Sharpening**

The field-directed sputter sharpening (FDSS) technique is a modified procedure descended from the conventional sputter erosion sharpening procedures detailed in Chapter 1. The process employs an energetic flux of inert gas ions directed along the axis of the probe wire. Under FDSS, the metallic probe is biased relative to a remote chamber reference potential (ground). Ions impinging upon the probe surface are deflected by the resulting electric potential gradient surrounding the probe apex, maximal around the regions of greatest curvature. As in conventional sputter erosion sharpening, FDSS employs the dependence of sputter yield on angle of incidence to produce the microscale probe structure, though this interaction is perturbed by controlled flux deviation at the probe apex.

Within the existing model of sputter erosion, the effects of field-direction can be explained in terms of its effect on surface diffusion processes near the probe apex. We will suggest in Chapter 3 that this effect may follow from the local reduction in average ion flux in the apex region that occurs when probe bias is increased. Additionally, the

influence of electric field on the dynamics of radiation or thermally induced surface diffusion may influence the sharpening process.<sup>40</sup>

## **2.2. Sharpening of Platinum Iridium Alloy Probes**

One common probe material employed for scanning tunneling microscopy is an alloy of platinum and iridium metal, commonly 90% platinum with alloyed iridium to improve physical properties of the material. Whereas the other typical probe material, tungsten, naturally oxidizes under ambient conditions, platinum remains stable and can therefore be transferred between vacuum systems, requiring only a moderate degas (~600 °C) upon evacuation. Additionally, platinum offers the benefit of an exceptionally high work function (5.64 eV), which facilitates improved patterning. Such advantages make platinum iridium alloy a commonly employed probe material, despite the rarity of its constituent metals. For the purpose of this thesis, the choice is particularly advantageous due to the need for ambient exposure prior to transmission electron microscope (TEM) characterization.

In this experiment, some platinum-iridium probes were commercially purchased from Materials Analytical Services (MAS) Incorporated (Suwanee, Georgia).<sup>46</sup> Where employed, these tips will be described as PtIr-MAS probes. A typical probe, shown in TEM micrograph in Figure 2.1, has a 100 nm radius of curvature and an agglomeration of surface contamination. This surface layer is believed to be carbon-based and to originate at the graphite counter electrode employed during preparation. In other experiments, platinum iridium probes are electrochemically etched in CaCl<sub>2</sub> solution.<sup>13</sup> Where employed, these probes will be described as etched PtIr probes.

### **2.1.1. Low flux sharpening of platinum iridium under neon bombardment**

In one experiment, a PtIr-MAS probe is characterized and then processed by FDSS. The probe is biased at 400 V relative to vacuum chamber ground while 2000 eV neon ions are directed along the axis of the probe wire. Several subsequent processing cycles are carried out under identical conditions, and the tip geometry is found to change significantly. A sequence of TEM micrographs is shown in Figure 2.2, in which the tip radius of curvature reduces from 100 nm to less than 1 nm, approaching atomic proportions. A direct comparison between apices is made in Figure 2.3, where each apex is identically scaled and shown in outline for parallel comparison.

Factors influencing this experiment beyond the application of probe bias include reduced ion current density, and the use of a lighter ion species. Both factors are expected to improve the sharpening effect in both control and experimental cases.

### **2.1.2. Control sharpening of platinum iridium alloy**

As a natural control, an etched PtIr probe is sharpened via conventional sputter sharpening by argon ions. Ion energies of 1.6 keV were employed with a grounded probe and the sputtering process proceeded for 10 h, adding assurance of equilibrium of form. As seen in Figure 2.4, the resulting probe is impressively sharp, but does not reach the scale achieved in the FDSS experimental case. The resulting radius of curvature is approximately 8 nm.

## **2.2. Sharpening of Tungsten Probes**

Polycrystalline tungsten probes are commonly employed in scanning tunneling microscopy due to their ease of preparation and low cost. Tungsten probes produced by NaOH electrochemical etch can be further sharpened with the field-directed sputter sharpening procedure, under conditions similar to those employed for platinum iridium alloy. As a disadvantage, the ambient exposure required for TEM characterization commonly results in the oxidation of the probe surface prior to analysis. This difficulty is eliminated if electron microscopy is foregone in favor of immediate transfer to ultrahigh vacuum. Results of scanning tunneling microscope characterization will be discussed in Chapter 4.

Several characteristic results of tungsten probe sharpening are provided in Figures 2.5 and 2.6. In each case, the probe radius is found to be significantly reduced from initial conditions, and such probe formation is found to be typical for similarly prepared probes. We find tungsten probe radii to fall within a range of 1-5 nm, generally an improvement over earlier results discussed in Chapter 1. It is believed that ambient exposure adversely affects these tungsten probes during transfer, resulting in oxide growth. This growth appears predominantly at the probe apex and is expected to result in detectable blunting of the probe prior to characterization.

## **2.3. Discussion**

The FDSS technique is found to produce exceptionally sharp probes and to be self-limiting and reproducible. Of note is the relative improvement when compared to the conventional sputter erosion technique. The radius of curvature for some probes was

found to approach the atomic scale, meeting or exceeding the 1.6 nm projected range for 1.6 keV argon in platinum reported by TRIM.<sup>47</sup> In general this range is expected to offer a lower bound for sharpening procedures, though a reduction of ion energy will reduce ion range, potentially facilitating a full reduction of probe dimensions to the atomic scale.

## 2.4. Figures

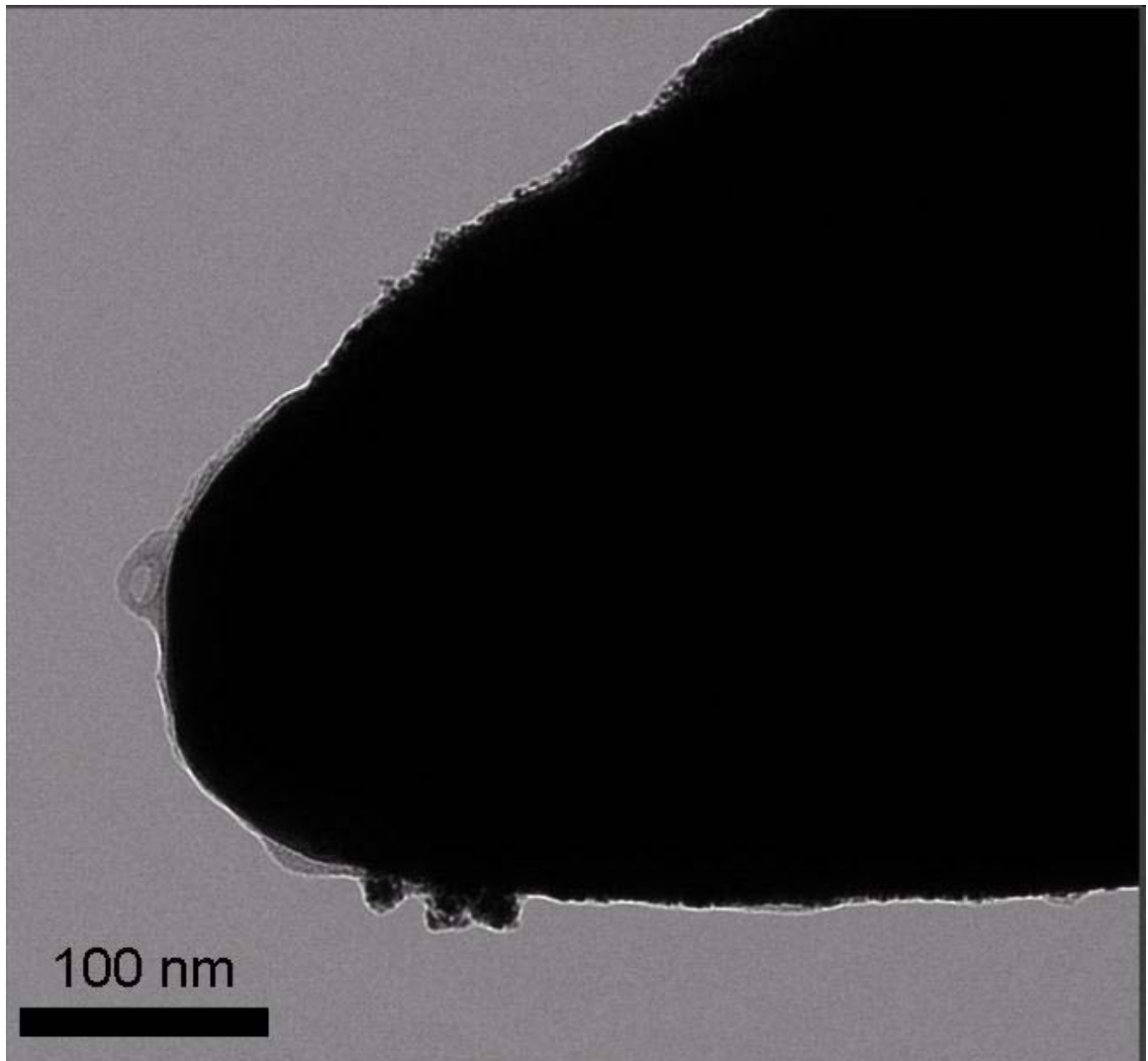


Figure 2.1: Transmission electron micrograph of a typical MAS PtIr probe. The radius of curvature is approximately 100 nm and a mild surface layer is visible.

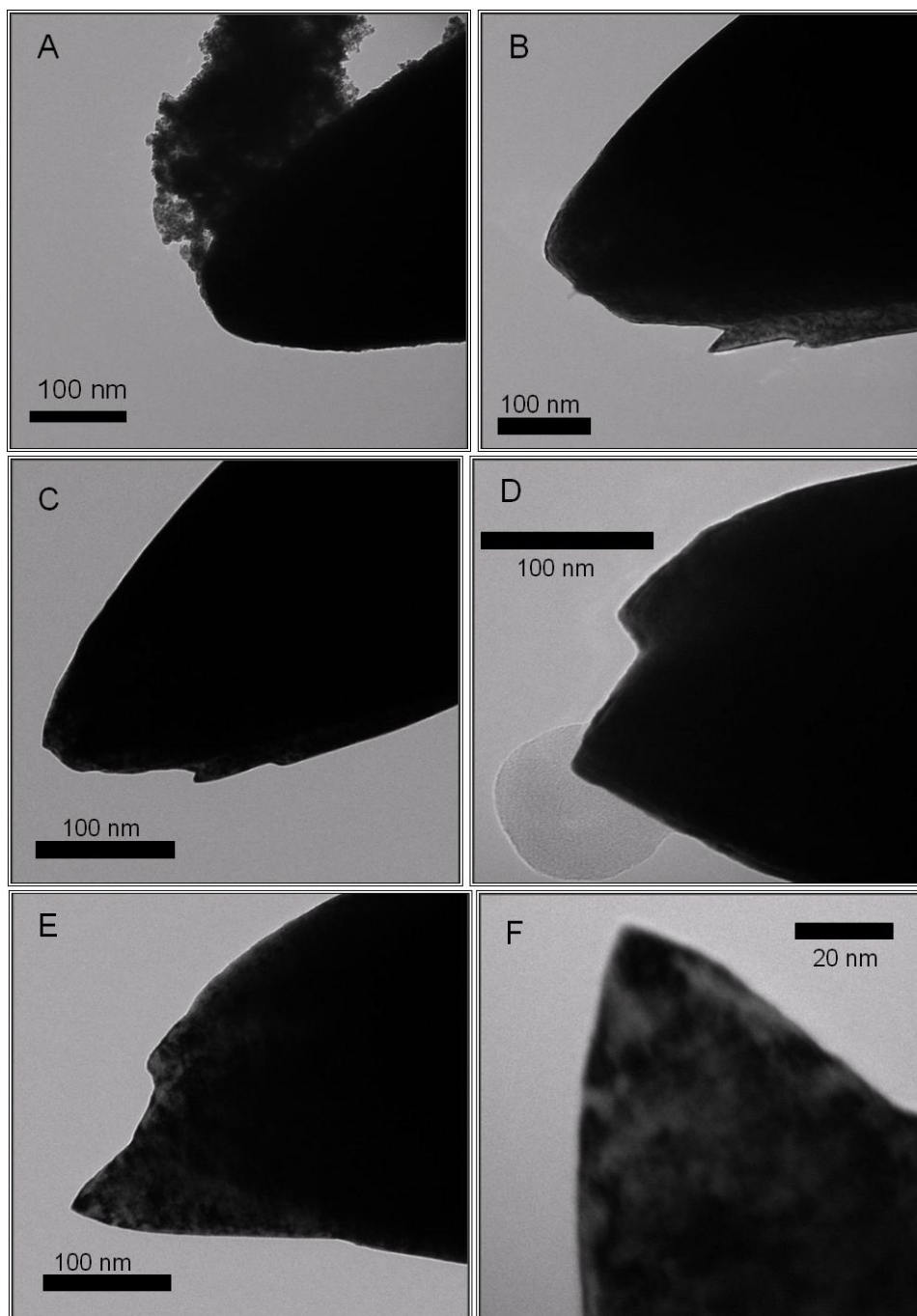


Figure 2.2: Sharpening progression of a MAS PtIr probe subjected to field-directed sputter sharpening. Ion energy of 2 keV and probe bias of 400 V were employed. 2.2A shows the initial probe form, 2.2B shows the probe following 75 min of erosion, 2.2C after 135 total min, 2.2D after 165 total min, 2.2E after 195 total min. Figure 2.2F shows a high resolution image of the tip seen in Figure 2.2E. The radius of curvature is shown to reduce to the single nanometer scale.

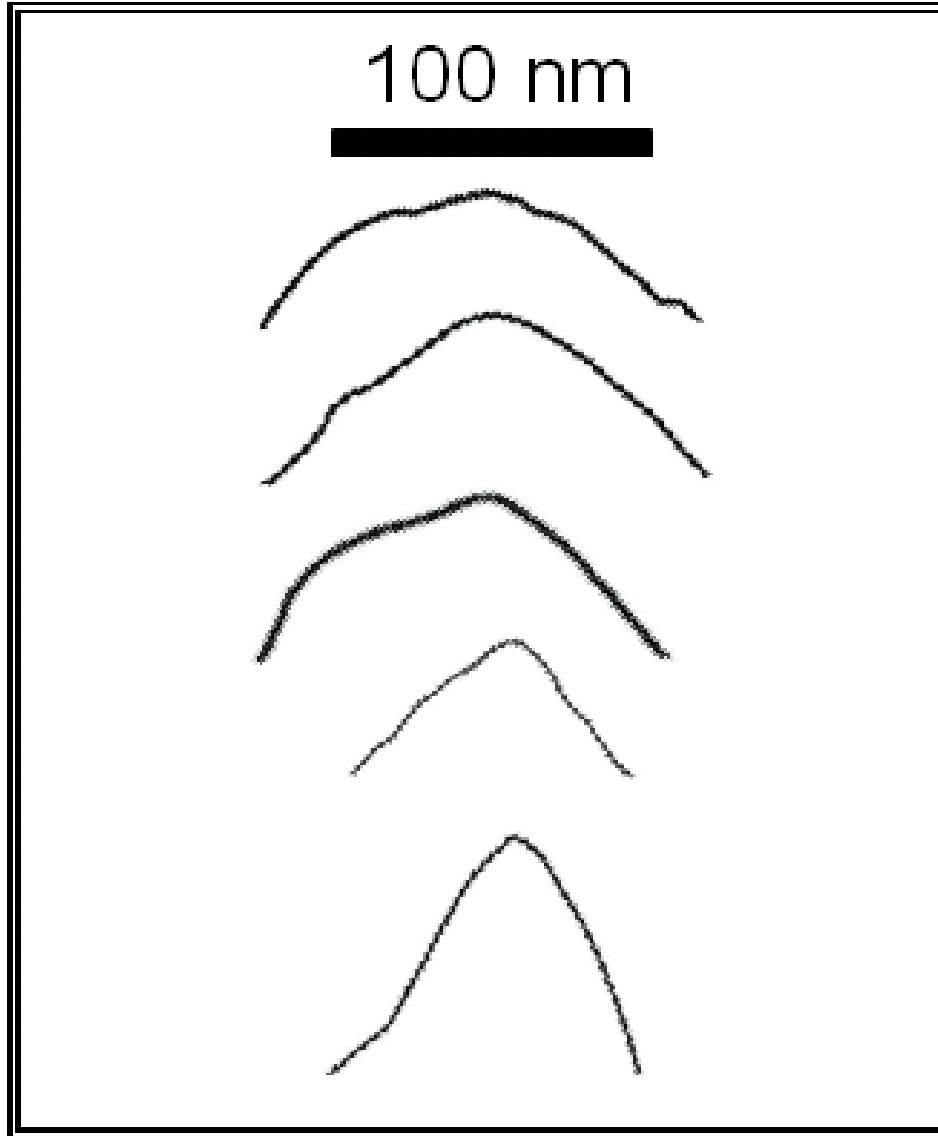


Figure 2.3: Scaled comparison between subsequent erosion stages of a platinum iridium probe subjected to field-directed sputter sharpening. Ion energy of 2 keV and probe bias of 400 V were employed.

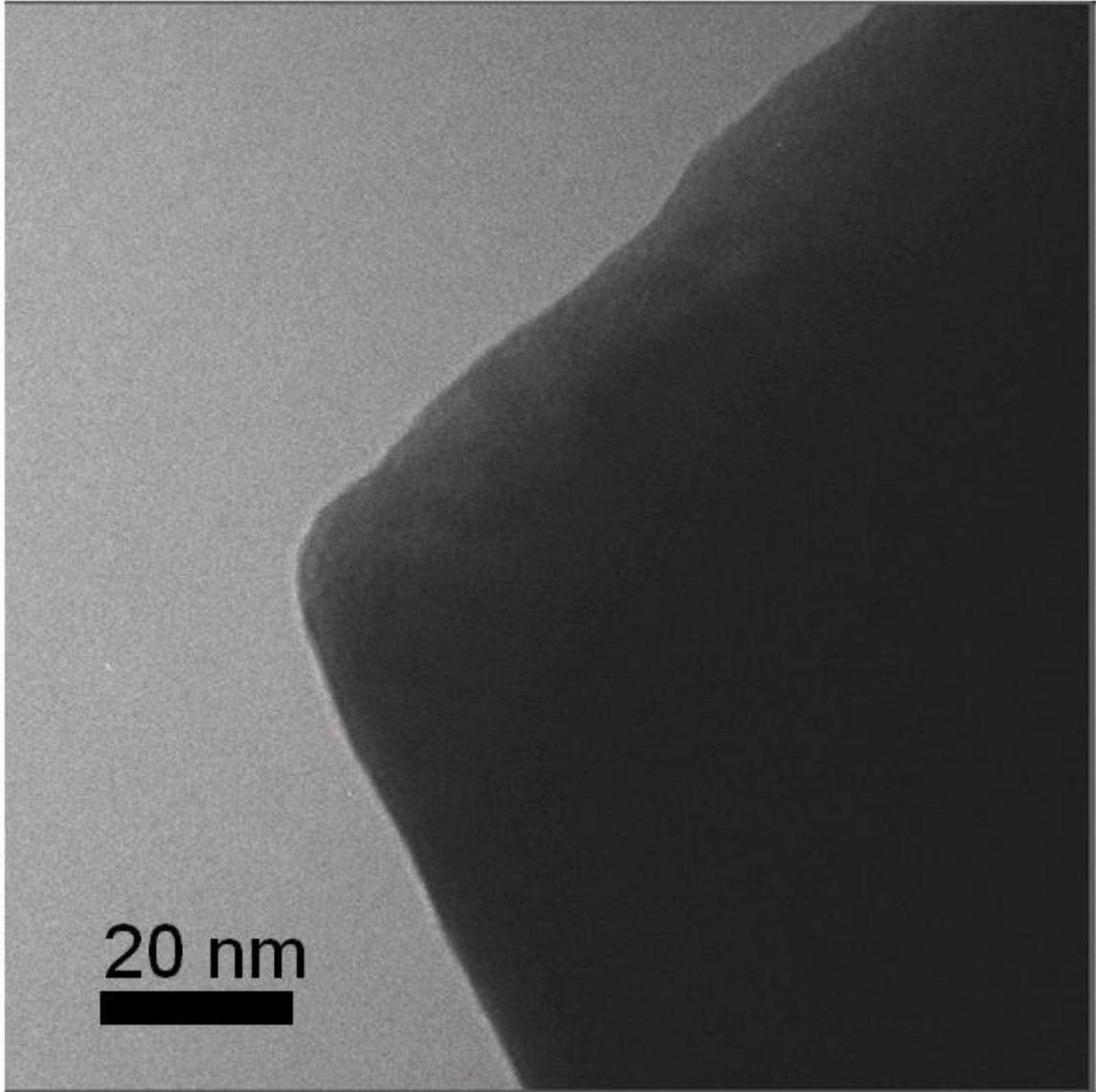


Figure 2.4: Platinum iridium alloy probe prepared by conventional sputter sharpening with 1.6 keV ions and grounded probe. The resulting probe has a radius of curvature of approximately 8 nm and a curiously large cone angle.

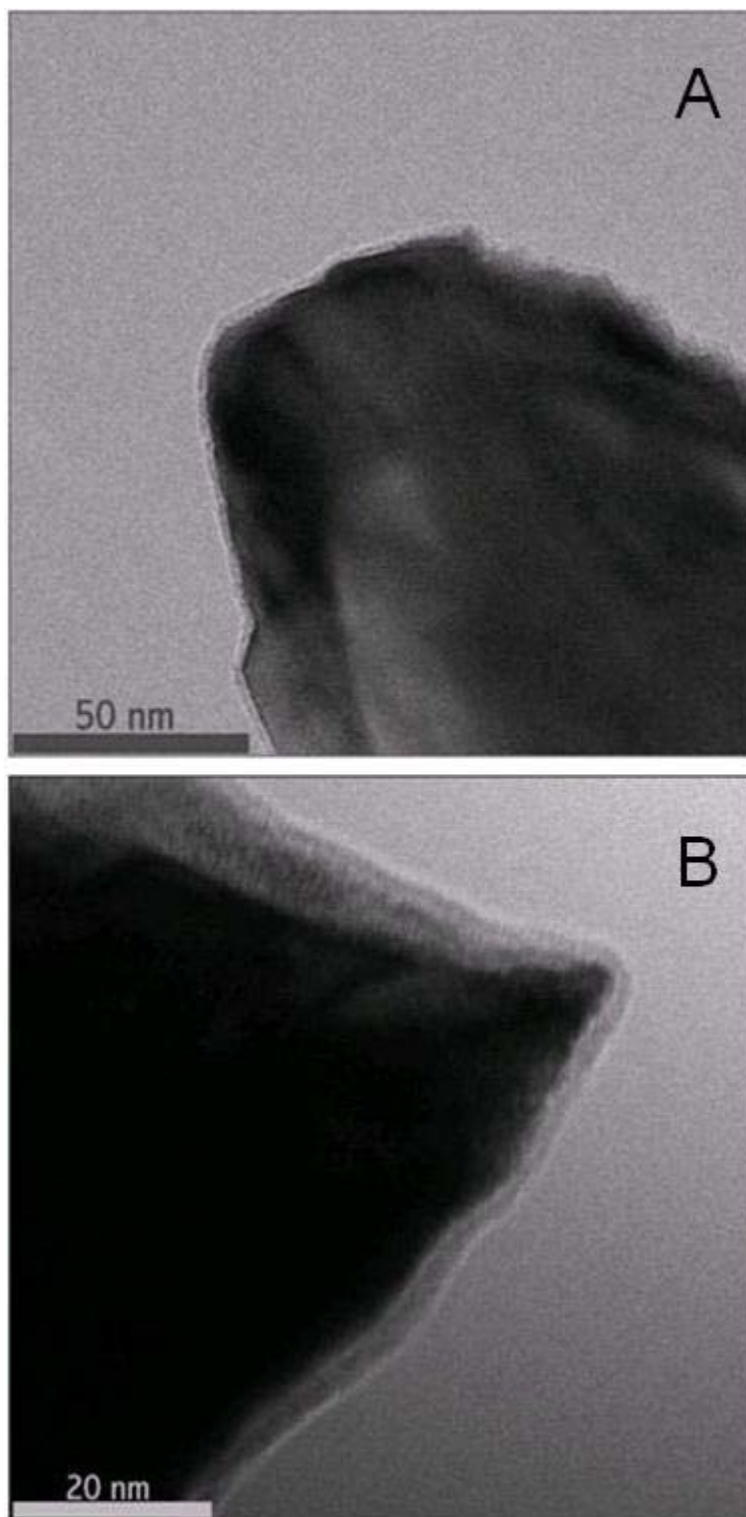


Figure 2.5: Demonstration of the field-directed sputter sharpening procedure on a polycrystalline tungsten probe. The initial probe is shown in Figure 2.5A. Ion energy was 2 keV and probe bias of 400 V was employed for 15 min. The final probe radius of curvature (Figure 2.5B) is 1-2 nm when measured at the subsurface tungsten layer.

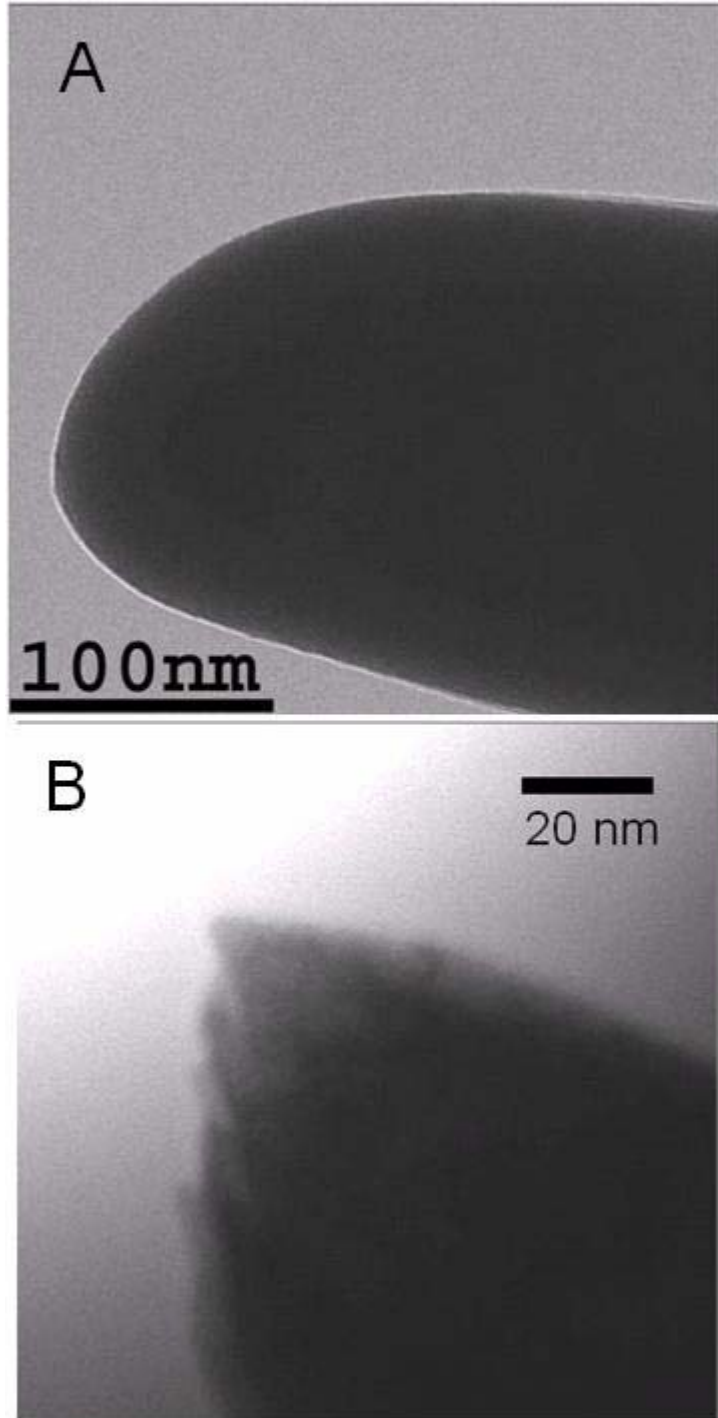


Figure 2.6: Further demonstration of polycrystalline tungsten sharpening. Ion energy of 2 keV was employed and a probe bias of 400 V was applied during sputtering, which proceeded for 35 min. The initial probe appears in Figure 2.6A and the probe following FDSS appears in 2.6B.

### **CHAPTER 3**

## **MECHANISM OF PROBE NANOSTRUCTURING UNDER FIELD-DIRECTED SPUTTER SHARPENING**

This chapter describes simulation of the field-directed sputter erosion process, describing the effects of electric field on ion action at the probe surface. Specifically, Section 3.1 considers the influence on an impinging ion beam of an applied bias to a simple infinite wire system, and Section 3.2 discusses variation with probe bias of average ion current density at the probe apex.

### **3.1. Local Influence of Probe Bias on Ion Path Trajectory**

The most intuitive model for field-directed sputter sharpening results directly from selective beam spreading at regions of enhanced electric field. At regions of increased surface curvature, the electric field is enhanced due to charge localization, a phenomenon which can be understood by application of Gauss's law to a surface at uniform electric potential. This field selectively repels the ion beam from the probe region while sputter erosion proceeds in the surrounding area. This image is appealing, but is insufficient to explain the improvements observed under applied probe bias when compared with conventional sputter sharpening. It is believed that sputter induced morphology changes, and specifically the resulting structure following edge formation, are dependent on surface diffusion phenomena.<sup>24,29</sup>

For convenience, we consider a simple probe model of an infinite conducting wire. The wire is an appealing choice of geometry in view of the future goal of modeling sputter erosion under the Sigmund model.<sup>23</sup> In this model the energy distribution is approximately Gaussian in space and integration over the infinite wire length provides an equivalently distributed Gaussian in a simplified two-dimensional

system. Nevertheless, for this computation we are concerned only with ion motion in the probe region.

It is understood that the electric potential of an ionized atom in the vicinity of a positively biased infinite wire can be described:

$$U(\vec{r})=U(r)=\frac{qV_tR_t}{r}\equiv\frac{k}{r} \quad (3.1)$$

Recognizing this system as a repulsive Kepler potential,<sup>48</sup> we can immediately write the hyperbolic ion path form for a probe centered at the origin:

$$\frac{1}{r}=C(e\cos(\theta-\theta_0)-1) \quad (3.2)$$

$$C=\frac{km}{L^2} \quad (3.3)$$

$$e=\sqrt{1+\frac{2EL^2}{mk^2}} \quad (3.4)$$

where  $m$  is the mass of the ion species employed,  $E$  is the initial ion energy (kinetic), and  $L$  is the angular momentum of the probe-ion system, given by

$$L=x_0\sqrt{2mE} \quad (3.5)$$

In the equations above,  $(r,\theta)$  are coordinates of the polar coordinate system, and  $\theta_0$  is a constant of integration, which can be determined from initial conditions. Specifically, assuming the ion approaches from an infinite distance,  $r$  becomes infinite for  $\theta$  approaching the surface normal ( $\pi/2$ ). Therefore, we can determine

$$\theta_0=\frac{\pi}{2}-\arccos\left(\frac{1}{e}\right)=\arcsin\left(\frac{1}{e}\right) \quad (3.6)$$

This simple solution of the Kepler problem for a repulsive spherical potential allows for the computation of ion paths for a variety of experimental conditions, as shown in Figure 3.1.

In further analysis we shall assume a uniform flux of ions. This approximation is reasonable on the length scale with which we are concerned, with probe radii on the order of 100 nm. As a result, one need only ask the range of initial ion positions for which probe impact results. In the simplest case, this relates to the initial position  $x_0$  for which ion impact occurs at a 90 degree angle of incidence. Any ion originating farther from the axis than  $x_0$  will not impact the sphere. To solve this problem, simply consider the state for which the ion path proceeds normal to the vector  $\mathbf{r}$ :

$$\frac{\partial r}{\partial \theta} = \frac{e \sin(\theta - \theta_0)}{C(e \cos(\theta - \theta_0) - 1)} = 0 \quad (3.7)$$

As  $C$  and the orbit eccentricity ( $e$ ) are both finite in this model, and the eccentricity is non-zero for a repulsive potential, this equation is solved where the sine term approaches zero, or equivalently:

$$\theta = \theta_0 = \arcsin\left(\frac{1}{e}\right) \quad (3.8)$$

Applying this restriction to Equation (3.2), we determine solutions for which this configuration occurs at the outer shell of our surface:

$$\frac{1}{r} = \frac{1}{R_t} = C\left(e \cos\left(\arcsin\left(\frac{1}{e}\right) - \arcsin\left(\frac{1}{e}\right)\right) - 1\right) = C(e - 1) \quad (3.9)$$

We reduce this equation and replace the ratio of probe bias to accelerating voltage as shown in Equation (3.10):

$$\frac{qV_t}{E} \equiv V_r \quad (3.10)$$

$$\sqrt{1 + \frac{4x_0^2}{V_r^2 R_t^2}} = \frac{2x_0^2}{R_t^2 V_r} + 1 \quad (3.11)$$

The solution to this equation is

$$x_0 = R_t \sqrt{1 - V_r} \quad (3.12)$$

### 3.2. Average Ion Flux over a Biased Cylindrical Conductor

From the results of Section 3.1, we can describe average ion current density over the modeled two-dimensional probe. As shown in Figure 3.2, the current originating in the region between zero and  $x_0$  is distributed in some, as yet unexplained, manner over the sphere surface. Ions originating outside this window are deflected and do not impact the probe. Under our assumption of uniform ion current density, we can describe the number of ions striking the probe:

$$N = \rho_{ion} x_0 \quad (3.13)$$

where  $\rho_{ion}$  is the density of ions originating at the ion source. Given a final probe radius below 5 nm, and the possible influence of thermal effects on the final probe dimension, it can be interesting to consider the energy dissipated on the sphere, and we therefore consider the distribution of these ions over the region of length  $R_t$ . The ratio of generated ion flux to surface ion flux is given by

$$\frac{\rho_{surf}}{\rho_{ion}} = \sqrt{1 - V_r} \quad (3.14)$$

We can then describe the ion flux at the probe surface for variable biasing conditions, described by  $V_r$ . A plot of this ion flux is provided in Figure 3.3.

### 3.3. Discussion

The reduction in average ion current density at the probe apex with increasing probe bias has been determined for a geometrically simple system, the infinite conductive cylinder. The ion current density is independent of probe radius, and varies as the root of the voltage ratio  $V_r$ . We believe that this offers one possible explanation for the field-directed sputter sharpening effect. It is suggested that a selective reduction of ion flux at a probe apex can result in selective reduction of surface diffusion at the apex, leading to minimized equilibrium probe dimensions. In this case, a similar effect might be achieved by a universal reduction in ion current density, with the additional effect of significantly increasing the time interval necessary for sharpening to proceed.

Alternatively, it is known that diffusion in an electric field gradient can influence the motion of surface atoms and counterbalance thermal diffusion effects.<sup>40</sup> Throughout this work no indication has been seen of accumulative growth of structure at the probe apex, a characteristic feature of such field-induced growth.<sup>41</sup> However, the study of field-directed sputter sharpening in a plasma etching environment may offer insight into this possibility.<sup>49</sup>

### 3.4. Figures

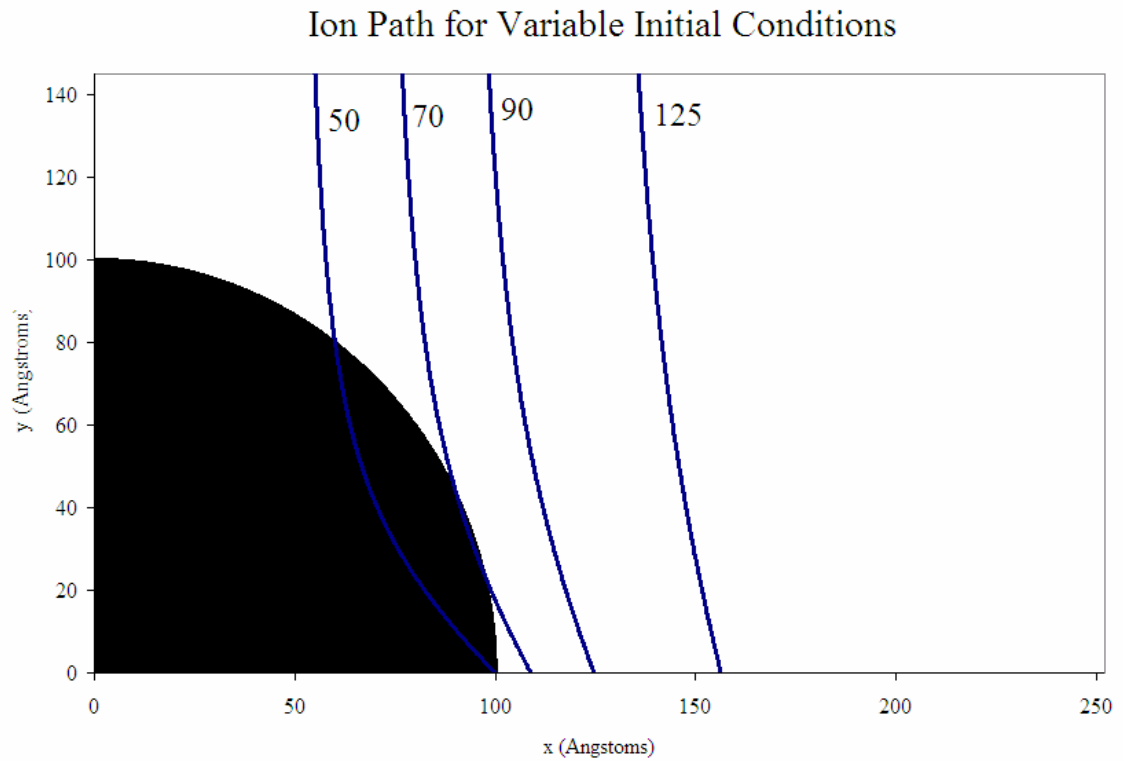


Figure 3.1: Simulation of several singly ionized argon ion paths over a biased probe. Probe bias is 1 kV with initial ion energy of 2 keV, for  $V_r=0.5$ . Initial ion positions are denoted in Angstroms (50, 70, 90, 125).

### Glancing Ion Impact Path

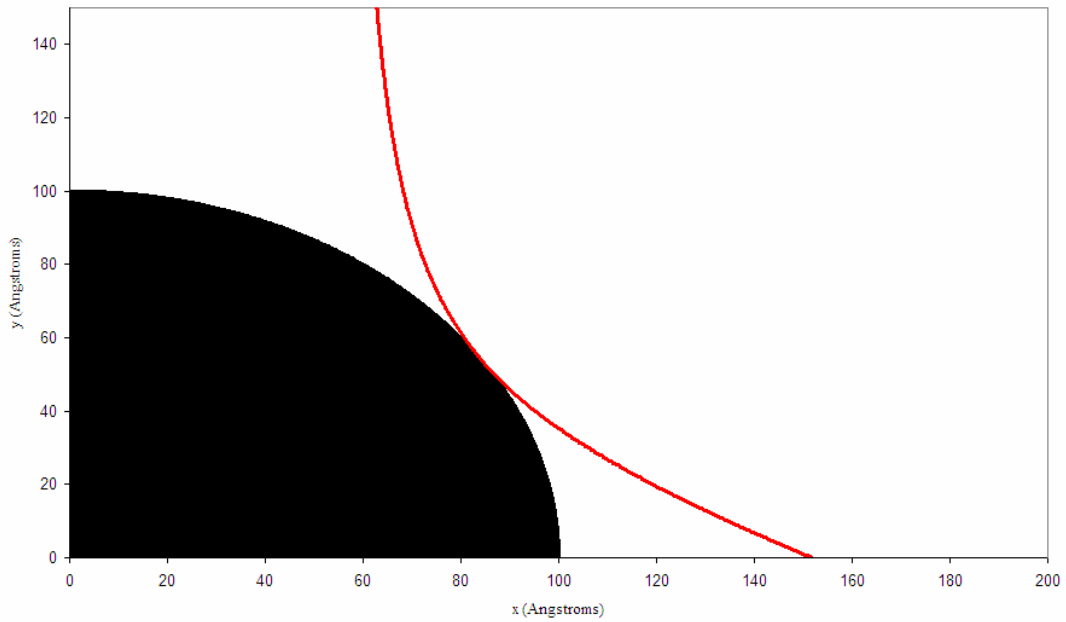


Figure 3.2: Calculated ion path for a glancing impact, as determined by Equation (3.12). In this system, ion energy was 2 keV, and the probe was biased to 1.4 keV. The radius of the spherical probe was fixed at 100 Å, and singly ionized argon ions were assumed.

### Normalized Apex Ion Current Density

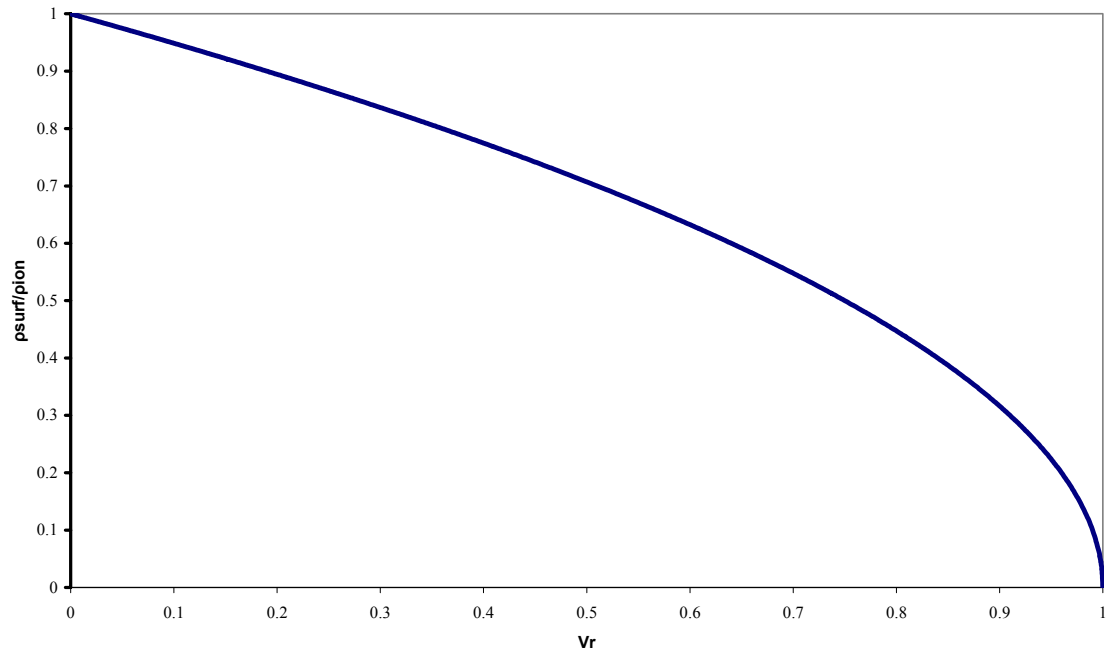


Figure 3.3: Calculated variation in normalized apex ion current density with the relative applied probe bias.  $V_r$  is defined in Equation (3.10) and the plot is derived from Equation (3.14).

## CHAPTER 4

### SCANNING TUNNELING MICROSCOPY AND HIGH FIDELITY ELECTRON-STIMULATED DESORPTION

The ability to employ probes prepared by field-directed sputter sharpening (FDSS) in the ultrahigh vacuum scanning tunneling microscope (UHV-STM) is of interest for purposes of precise substrate modification. Specifically, FDSS probes are shown to produce exceptional electron-stimulated desorption<sup>3</sup> patterns on the hydrogen passivated Si(100) 2x1 reconstructed surface [Si(100) 2x1:H].

In addition to the imaging capabilities of the STM, it offers the potential for selective chemical structuring of the substrate surface. In this case, electrons tunneling from tip to surface will be employed for the selective desorption of hydrogen. This process can be performed either as a single electron process in the field emission regime by directly elevating the bonding electron to the antibonding state, or via a vibrational heating mechanism at lower electron energies.<sup>50</sup>

#### 4.1. High Fidelity Patterning of the Si(100) 2x1:H Surface

Following sharpening of a tungsten probe, the STM provides an excellent tool for characterization. Though use in the STM can be a significantly more subjective measure of probe quality, as it is the ultimate goal of this experiment it is arguably the best possible metric. As the spatial distribution of the electron tunneling current is dependent on the probe radius,<sup>51</sup> electron-stimulated patterning offers a reasonable technique for probe apex characterization. The quality of FDSS probes in STM can be demonstrated by high resolution imaging, but more importantly by high fidelity patterning of the

hydrogen passivated silicon surface. In Figure 4.1, a high resolution image of the Si(100) 2x1:H surface is shown. Though it is not necessary to perform extensive sharpening procedures to achieve such resolution, the result demonstrates clearly an ability to employ the resulting probe for STM and suggests the absence of significant amounts of radiation-induced crystal damage as a source of instability.

Additionally, patterning of the silicon surface by electron-stimulated desorption of hydrogen was performed, and the result shown in Figure 4.2. The high fidelity patterns produced suggest a small probe apex with correspondingly narrow tunneling current distribution.

#### **4.2. Probe Regeneration by Field-Directed Sputter Sharpening**

While operating within the STM, probes commonly undergo structural changes due, for example, to surface diffusion or mechanical contact with the substrate under analysis. Though the result of a “tip change” can be advantageous, for instance by the creation of an atomically sharp point, more frequently imaging resolution suffers. Often disadvantageous changes are reversible, though the recovery process is rarely deterministic, and commonly involves aggressive tip actions until further structural modification occurs.

Unfortunately, scanned probes remain a consumable item. However, for mildly damaged probes, regeneration by FDSS may be possible. In this experiment, a polycrystalline tungsten probe was employed in the STM for imaging and patterning of the silicon surface. Following extended scanning, the probe sustained damage and was unable to provide precise patterning. Figure 4.3 includes a representative pattern

produced by the degraded probe. Though some evidence of atomic-scale surface structure can be discerned, the electron-stimulated desorption patterns are broadened. Additionally, the probe appears to have multiple apices, each of which is providing an STM image of the surface in parallel. As a result, multiple shadow images are visible on the surface for each line. It was determined that the damaged probe used to generate Figure 4.3 would be a good candidate for regeneration via FDSS. Without removal from high vacuum, the probe was subjected to FDSS processing with ion energies of 1.2 keV and a probe bias of 200 V. The probe was not imaged by transmission electron microscopy, but immediately returned to ultrahigh vacuum for further use in the STM.

The regenerated tip enabled stable imaging of the silicon surface, and high fidelity patterning by electron-stimulated desorption. One representative pattern is demonstrated in Figure 4.4. Of particular interest is the extreme patterning precision visible in this image. Outside of the immediate patterns, which follow the atomic dimers of the surface, most dangling bonds are randomly distributed and due to imperfect sample preparation, as opposed to electron-stimulated desorption.

### 4.3. Figures

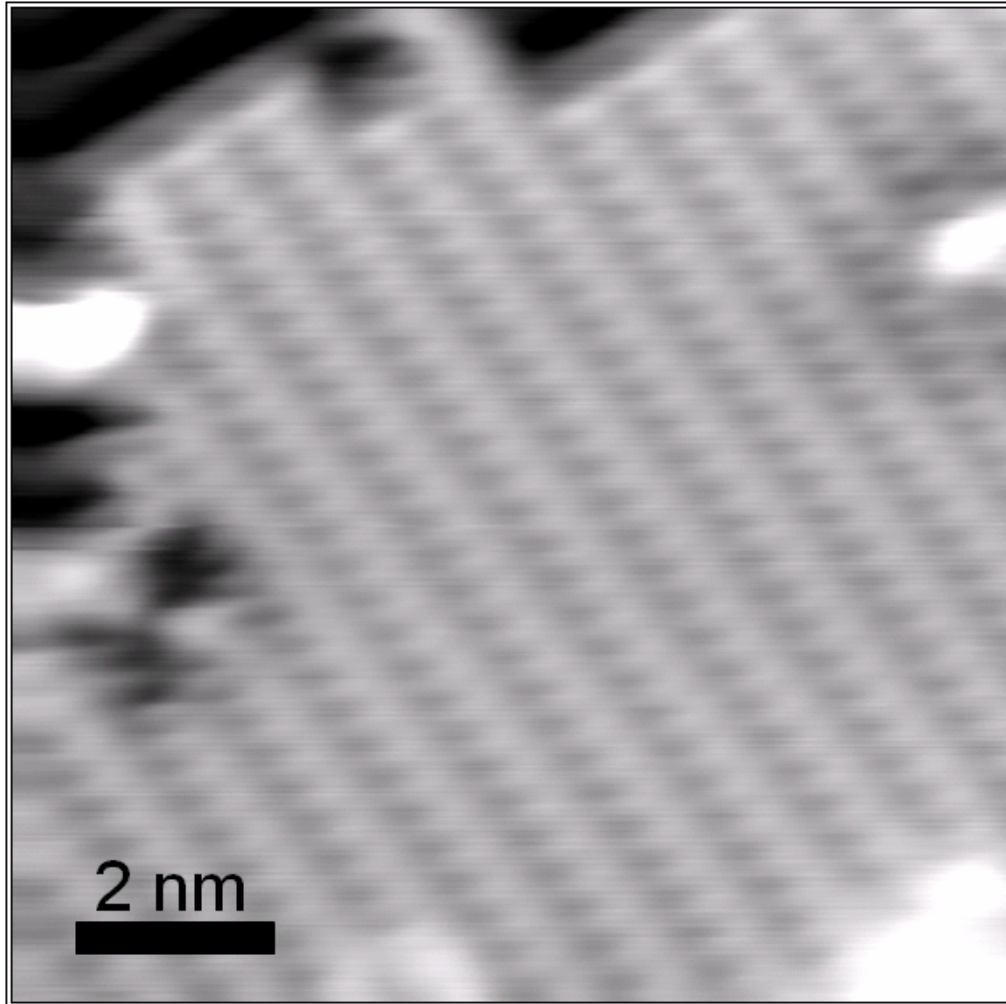


Figure 4.1: Dimer resolution imaging of the silicon(100) 2x1:H surface using a tungsten tip processed with field-directed sputter sharpening. Imaging performed with a -2 V sample bias and 50 pA tunneling current setpoint.

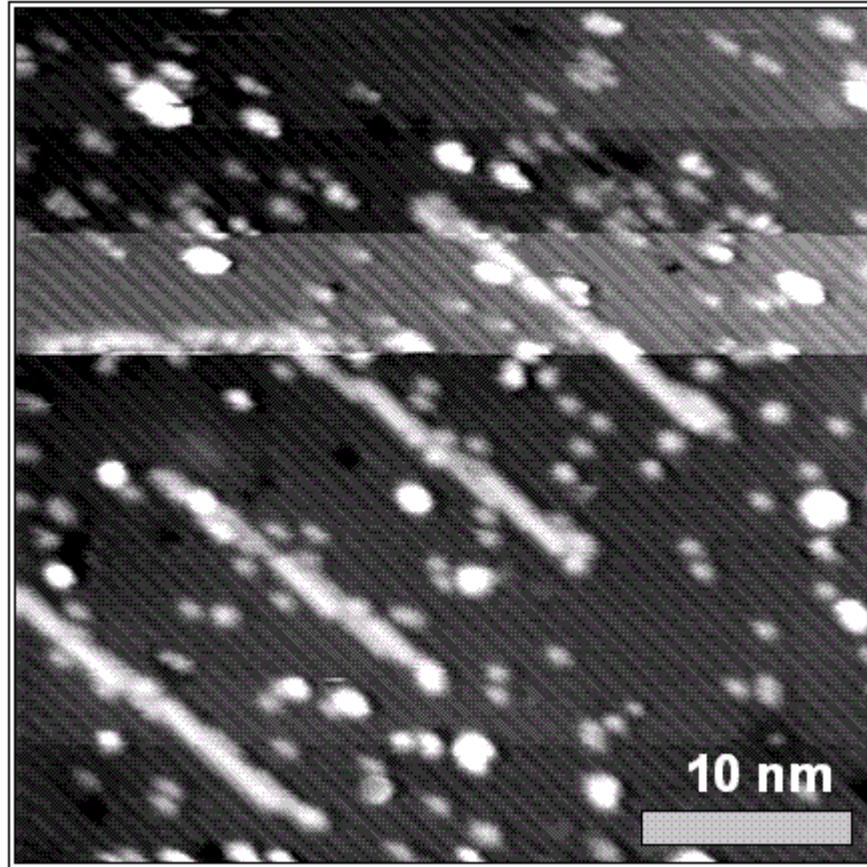


Figure 4.2: Electron-stimulated desorption patterning of the Si(100) 2x1:H surface performed by polycrystalline tungsten FDSS probe. Noteworthy features include the relative absence of spurious depassivation events, outside the background of mild defects related to sample preparation. Also, the slight variation in tip that occurs during the scan is worthy of note. It cannot be claimed that FDSS probes are more resilient than their etched counterparts of equivalent material. Tip instability can occur, but here will rarely occur as a result of unstable adsorbates on the probe surface. Imaging was done with a sample bias of -2 V and tunneling current of 50 pA. Patterning was done with a sample bias of +4 V, a tunneling current of 2 nA, and dose of  $2 \times 10^{-3}$  coulombs/cm.

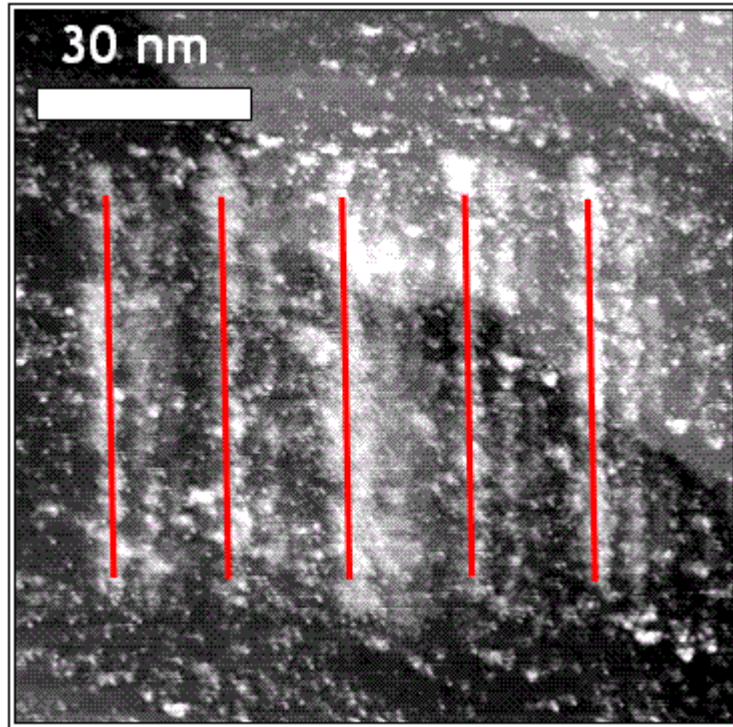


Figure 4.3: STM topographic data for electron-stimulated desorption patterns on the hydrogen passivated Si(100) 2x1 surface. Scanning bias of -2 V and tunneling current 50 pA were employed for imaging. During patterning a sample bias of +4 V and tunneling current of 2 nA were employed, the tip velocity during patterning provided a line dose of  $2 \times 10^{-3}$  coulombs/cm. Silicon dimers and two atomic steps are visible, but patterns are broadened and tip multiplicity is apparent. Red lines correspond to the probe path followed during the depassivation cycle.

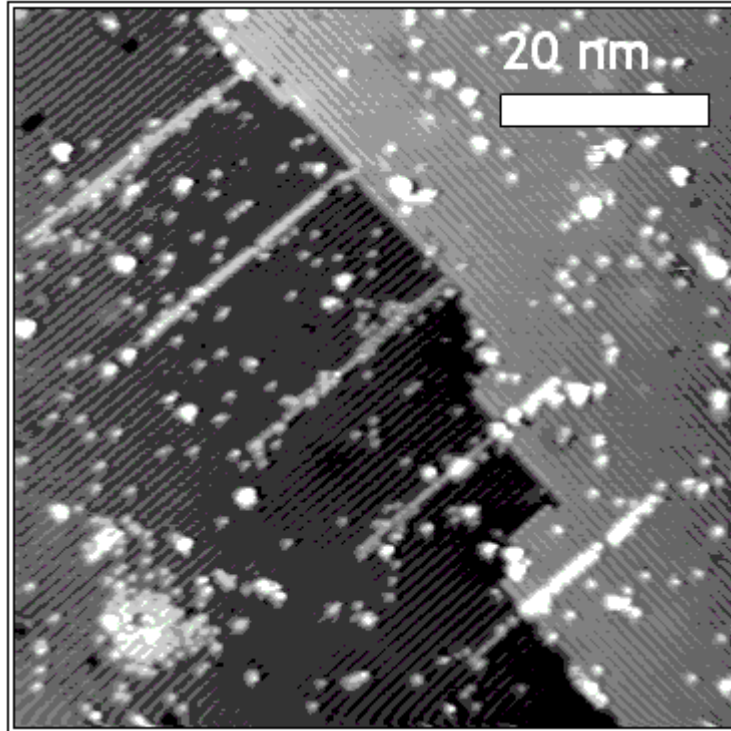


Figure 4.4: STM topographic data collected on the Si(100) 2x1:H surface following FDSS probe regeneration with ion energy of 1.2 keV and probe bias of 200 V. During scanning, sample bias of -2 V and tunneling current of 50 pA were employed. During patterning a sample bias of +4 V and tunneling current of 2 nA were employed. The tip velocity provided a line dose of  $2 \times 10^{-3}$  coulombs/cm. The circular feature in the lower left is a deliberate broad depassivation site created by a pause of the tip while under patterning conditions. Many of the bright features in this image are dangling silicon bonds created by an imperfect sample preparation cycle. Several of these depassivation sites have been bound to adsorbed molecules, which serve as surface contaminants. The patterned lines are of extremely high fidelity, generally following the silicon dimer surface structure with few spurious atomic desorption events.

## CHAPTER 5

### CONCLUSIONS AND FUTURE WORK

In this thesis we have demonstrated the ability to sharpen tungsten and platinum iridium alloy probes to nanometer and sub-nanometer proportions by a novel technique termed field-directed sputter sharpening. The resulting probes were shown by transmission electron microscopy to include reduced radii of curvature when compared with their classically sputter eroded counterparts. The exact mechanism for this sharpening procedure is not known, but two possible influences have been identified which may encourage such an effect. First, we have modeled the reduction of ion flux in the vicinity of a biased probe under the assumption of an isolated conductive wire. A reduction in ion flux will reduce radiation induced and thermally induced surface diffusion, which is expected to reduce the equilibrium probe radius of curvature. Alternatively, the field enhancement occurring at the probe apex will influence the flux of diffusing surface ions, which may result in an additional sharpening effect. Further work is necessary to distinguish these effects, or potentially to determine additional factors involved.

Field-directed sputter sharpening promises scalability, even to the wafer scale. Further exploration of this scaling process, perhaps through plasma processing, is an intriguing focus for further study.

A distinguishing characteristic of sputter erosion sharpening is its applicability across material systems. The anticipated ability to apply field-directed sputter sharpening to novel materials for which chemical sharpening procedures are not readily

available promises exciting opportunities for novel probes. By selecting material properties of interest, experimental conditions can be tailored for the material system being studied. Films of ultra-hard material might provide increased mechanical stability in scanned probe applications. Selection of electronically favorable materials might facilitate nanoscale electrical contacts to molecules or devices, including carbon nanotubes or graphene nanoribbons. With proper material selection, controlled deposition from probe to sample of probe material or of probe adsorbates may be facilitated.

Additionally, the goal of patterning with reliable atomic precision is likely to be achievable and field-directed sputter sharpening promises reproducibility and regenerability for such a task. Even the ideal probe can promise only a finite life expectancy, and the prospect of in situ regeneration of such probes is exciting. By full exploration of the parameter space for field-directed sputter sharpening, it is possible that predictable, reproducible, atomically precise patterning of the silicon-hydrogen system and others will be achievable even to the micron scale.

## REFERENCES

- <sup>1</sup>G. Binnig, H. Rohrer, C. Gerber, and E. Weibel, *Phys. Rev. Lett.* **49**, 57 (1982).
- <sup>2</sup>G. Binnig, C. F. Quate, and C. Gerber, *Phys. Rev. Lett.* **56**, 930 (1982).
- <sup>3</sup>J. W. Lyding, T. C. Shen, J. S. Hubacek, J. R. Tucker, and G. C. Abeln, *Appl. Phys. Lett.* **64**, 2010 (1994).
- <sup>4</sup>M. C. Hersam, N. P. Guisinger, and J. W. Lyding, *Nanotechnology* **11**, 70 (2000).
- <sup>5</sup>S. R. Schofield, N. J. Curson, M. Y. Simmons, F. J. Rueß, T. Hallam, L. Oberbeck, and R. G. Clark, *Phys. Rev. Lett.* **91**, 13 (2003).
- <sup>6</sup>M. B. Haider, J. L. Pitters, G. A. DiLabio, L. Livadaru, J. Y. Mutus, and R. A. Wolkow, *Phys. Rev. Lett.* **102**, 046805 (2009).
- <sup>7</sup>A. V. Crewe, D. N. Eggenberger, J. Wall, and L. M. Welter, *Rev. Sci. Instrum.* **39**, 576 (1968).
- <sup>8</sup>O. Auciello, L. Yadon, D. Temple, J. E. Mancusi, G. E. McGuire, E. Hirsch, H. F. Gray, and C. M. Tang, in *Eighth International Vacuum Microelectronics Conference*, Portland, Oregon, 1995, pp. 192-196.
- <sup>9</sup>E. Stoll, *Surf. Sci.* **143**, L411 (1984).
- <sup>10</sup>T. T. Tsong, *Atom-Probe Field Ion Microscopy: Field Ion Emission and Surfaces and Interfaces at Atomic Resolution* (Cambridge University Press, Cambridge, 1990), p. 387.
- <sup>11</sup>A. J. Melmed, *J. Vac. Sci. Technol. B* **9**, 601 (1991).
- <sup>12</sup>S. Morishita and F. Okuyama, *J. Vac. Sci. Technol. A* **9**, 167 (1991).
- <sup>13</sup>A. J. Nam, A. Teren, T. A. Lusby, and A. J. Melmed, *J. Vac. Sci. Technol. B* **13**, 1556 (1995).
- <sup>14</sup>M. O. Watanabe and T. Kinno, *Jpn. J. Appl. Phys.* **32**, 1266 (1993).
- <sup>15</sup>M. Iwami, Y. Uehara, and S. Ushioda, *Rev. Sci. Instrum.* **69**, 4010 (1998).
- <sup>16</sup>P. J. Bryant, H. S. Kim, Y. C. Zheng, and R. Yang, *Rev. Sci. Instrum.* **58**, 1115 (1987).

- <sup>17</sup>J. P. Ibe, P. P. Bey Jr, S. L. Brandow, R. A. Brizzolara, N. A. Burnham, D. P. Dilella, K. P. Lee, C. R. K. Marrian, and R. J. Colton, *J. Vac. Sci. Technol. A* **8**, 3570 (1990).
- <sup>18</sup>R. Morgan, *J. Sci. Instrum.* **44**, 808 (1967).
- <sup>19</sup>A. Gunterschulze and W. V. Tollmien, *Z. Phys.* **119**, 685 (1942).
- <sup>20</sup>P. Sigmund, *Phys. Rev.* **184**, 383 (1969).
- <sup>21</sup>D. J. Barber, F. C. Frank, M. Moss, J. W. Steeds, and I. S. T. Tsong, *J. Mater. Sci.* **8**, 1030 (1973).
- <sup>22</sup>G. Carter, J. S. Colligon, and M. J. Nobes, *J. Mater. Sci.* **8**, 1481 (1973).
- <sup>23</sup>P. Sigmund, *J. Mater. Sci.* **8**, 1545 (1973).
- <sup>24</sup>G. Carter, *J. Mater. Sci.* **11**, 1091 (1976).
- <sup>25</sup>G. Carter, J. S. Colligon, and M. J. Nobes, *Radiat. Eff. Defects Solids* **31**, 65 (1977).
- <sup>26</sup>G. Carter, M. J. Nobes, and R. P. Webb, *J. Mater. Sci.* **16**, 2091 (1981).
- <sup>27</sup>J. A. Kubby and B. M. Siegel, *J. Vac. Sci. Technol. B* **4**, 120 (1986).
- <sup>28</sup>J. A. Kubby, Ph.D. dissertation, Cornell University, 1986.
- <sup>29</sup>R. M. Bradley and J. M. E. Harper, *J. Vac. Sci. Technol. A* **6**, 2390 (1988).
- <sup>30</sup>P. Hoffrogge, H. Kopf, and R. Reichelt, *J. Appl. Phys.* **90**, 5322 (2001).
- <sup>31</sup>Q. Wang, C. Z. Gu, Z. Xu, J. J. Li, Z. L. Wang, X. D. Bai, and Z. Cui, *J. Appl. Phys.* **100**, 034312 (2006).
- <sup>32</sup>J. A. Kubby and B. M. Siegel, *Nucl. Instrum. Methods Phys. Res., Sect. B* **13**, 319 (1986).
- <sup>33</sup>C. Schiller, A. A. Koomans, T. L. Vanrooy, C. Schonenberger, and H. B. Elswijk, *Surf. Sci.* **339**, L925 (1995).
- <sup>34</sup>G. Wehner, *J. Appl. Phys.* **30**, 1762 (1959).
- <sup>35</sup>H. Fetz, *Z. Phys. A: Hadrons Nucl.* **119**, 590 (1942).

- <sup>36</sup>F. C. Frank, in *Growth and Perfection of Crystals*, Proceedings of an International Conference on Crystal Growth, Cooperstown, New York, 1958, edited by R. H. Doremus, B. W. Roberts, and D. Turnbull (John Wiley, New York, 1958), pp. 411–419.
- <sup>37</sup>F. C. Frank, *Z. Phys. Chem. Neue Folge* **77**, 84 (1972).
- <sup>38</sup>H. H. Anderson and H. L. Bay, in *Sputtering by Particle Bombardment I*, edited by R. Behrisch (Springer-Verlag, Berlin, 1981), p. 145.
- <sup>39</sup>I. H. Wilson and M. W. Kidd, *J. Mater. Sci.* **6**, 1366 (1971).
- <sup>40</sup>J. Y. Cavaille and M. Drechsler, *Surf. Sci.* **75**, 342 (1978).
- <sup>41</sup>V. Gill, P. R. Guduru, and B. W. Sheldon, *Int. J. Solids Structures* **45**, 943 (2008).
- <sup>42</sup>J. W. Lyding, S. Skala, J. S. Hubacek, R. Brockenbrough, and G. Gammie, *Rev. Sci. Instrum.* **59**, 1897 (1988).
- <sup>43</sup>R. T. Brockenbrough and J. W. Lyding, *Rev. Sci. Instrum.* **64**, 2225 (1993).
- <sup>44</sup>J. R. Janninck, M.S. thesis, University of Illinois at Urbana-Champaign, 1994
- <sup>45</sup>M. M. Sztelle, M.S. thesis, University of Illinois at Urbana-Champaign, 2002.
- <sup>46</sup>Material Analytical Services, <http://www.mastest.com/>.
- <sup>47</sup>J. F. Ziegler, U. Littmark, and J. P. Biersack, *The Stopping and Range of Ions in Solids* (Pergamon, New York, 1985).
- <sup>48</sup>B. Cordani, *The Kepler Problem: Group Theoretical Aspects, Regularization and Quantization, with Application to the Study of Perturbations* (Birkhäuser Verlag, Basel, 2003).
- <sup>49</sup>E. Lee, M.S. thesis, University of Illinois at Urbana-Champaign, 2009.
- <sup>50</sup>T. C. Shen, C. Wang, G. C. Abeln, J. R. Tucker, J. W. Lyding, P. Avouris, and R. E. Walkup, *Science* **268**, 1590 (1995).
- <sup>51</sup>T. M. Mayer, D. P. Adams, and B. M. Marder, *J. Vac. Sci. Technol. B* **14**, 2438 (1996).

## **AUTHOR'S BIOGRAPHY**

Scott W. Schmucker was born in Fayetteville, North Carolina, on June 30, 1982, and was raised in Mentor, Ohio. He graduated in 2004 from Case Western Reserve University with a degree in computer engineering. During his undergraduate years he participated in undergraduate research experiences at NASA Glenn Research Center, Cleveland, Ohio. In 2004 Scott was awarded the National Science Foundation Graduate Research Fellowship, National Defense Science and Engineering Graduate Fellowship and Tau Beta Pi Graduate Fellowship, and he relocated to Champaign, Illinois, where he began graduate study at the University of Illinois at Urbana-Champaign. At Illinois, Scott worked under the guidance of Professor Joseph Lyding in the field of electrical engineering with a focus on scanning tunneling microscopy and nanotechnology.